1
Fundamentals of Semiconductor Electrochemistry and Photoelectrochemistry

Krishnan Rajeshwar
The University of Texas at Arlington, Arlington, Texas

1.1 Introduction and Scope

The study of semiconductor–electrolyte interfaces has both fundamental and practical incentives. These interfaces have interesting similarities and differences with their semiconductor–metal (or metal oxide) and metal–electrolyte counterparts. Thus, approaches to garnering a fundamental understanding of these interfaces have stemmed from both electrochemistry and solid-state physics perspectives and have proven to be equally fruitful. On the other hand, this knowledge base in turn impacts many technologies, including microelectronics, environmental remediation, sensors, solar cells, and energy storage. Some of these are discussed elsewhere in this volume.

It is instructive to first examine the historical evolution of this field. Early work in the fifties and sixties undoubtedly was motivated by application possibilities in electronics and came on the heels of discovery of the first transistor. Electron transfer theories were also rapidly evolving during this period, starting from homogeneous systems to heterogeneous metal-electrolyte interfaces leading, in turn, to semiconductor-electrolyte junctions. The 1973 oil embargo and the ensuing energy crisis caused a dramatic spurt in studies on semiconductor–electrolyte interfaces once the energy conversion possibilities of the latter were realized. Subsequent progress at both fundamental and applied levels in the late eighties and nineties has been more gradual and sustained. Much of this later research has been spurred by technological applicability in environmental remediation scenarios. Very recently, however, renewed interest in clean energy sources that are nonfossil in origin, has provided new impetus to the study of semiconductor–electrolyte interfaces. As we also learn to understand and manipulate these interfaces at an increasingly finer (atomic) level, new microelectronics application possibilities may emerge, thus completing the cycle that first began in the 1950s.

The ensuing discussion of the progress that has been made in this field mainly hinges on studies that have appeared since about 1990. Several review articles and chapters have appeared since then that deal with semiconductor–electrolyte interfaces [1–10]; aspects related to electron transfer are featured in several of these. This author is also aware of at least three books/monographs/proceedings volumes that have appeared since 1990 [11–13]. The

reader is referred to the many authoritative accounts that exist before this time frame for a thorough coverage of details on semiconductor–electrolyte interfaces in general. Entry to this early literature may be found in the references cited earlier. In some instances, however, the discussion that follows necessarily delves into research dating back to the 1970s and 1980s.

To facilitate a self-contained description, we will start with well-established aspects related to the semiconductor energy band model and the electrostatics at semiconductor–electrolyte interfaces in the "dark". We shall then examine the processes of light absorption, electron-hole generation, and charge separation at these interfaces. The steady state and dynamic aspects of charge transfer are then briefly considered. Nanocrystalline semiconductor films and size quantization are then discussed as are issues related to electron transfer across chemically modified semiconductor–electrolyte interfaces. Finally, we shall introduce the various types of photoelectrochemical devices ranging from regenerative and photoelectrolysis cells to dye-sensitized solar cells.

1.2 Electron Energy Levels in Semiconductors and Energy Band Model

Unlike in molecular systems, semiconductor energy levels are so dense that they form, instead of discrete molecular orbital energy levels, broad energy bands. Consider a solid composed of N atoms. Its frontier band will have $2N$ energy eigenstates, each with an occupancy of two electrons of paired spin. Thus, a solid having atoms with odd number of valence electrons (e.g. Al with $[Ne]3s^2 3p^1$) will have a partially occupied frontier band in which the electrons are delocalized. On the other hand, a solid with an even number of valence electrons (e.g. Si having an electron configuration of $[Ne]3s^2 2p^2$) will have a fully occupied frontier band (termed a valence band, (VB)). The situation for Si is schematized in Fig. 1.

As Fig. 2 illustrates, the distinction between semiconductors and insulators is rather arbitrary and resides with the magnitude of the energy band gap (E_g) between the filled and vacant bands. Semiconductors typically have E_g in the 1 eV–4 eV range (Table 1). The vacant frontier band is termed a conduction band, (CB) (Fig. 2). We shall see later that E_g has an important bearing on the optical response of a semiconductor.

For high density electron ensembles such as valence electrons in metals, Fermi statistics is applicable. In a thermodynamic sense, the Fermi level, E_F (defined at 0 K

Tab. 1 Some elemental and compound semiconductors for photoelectrochemical applications

Semiconductor	*Conductivity type(s)*	*Optical band gap energy [eV]*[a]
Si	*n*, *p*	1.11
GaAs	*n*, *p*	1.42
GaP	*n*, *p*	2.26
InP	*n*, *p*	1.35
CdS	*n*	2.42
CdSe	*n*	1.70
CdTe	*n*, *p*	1.50
TiO_2	*n*	3.00 (rutile) 3.2 (anatase)
ZnO	*n*	3.35

[a] The values quoted are for the bulk semiconductor. The gap energies increase in the size quantization regime (see Sect. 7).

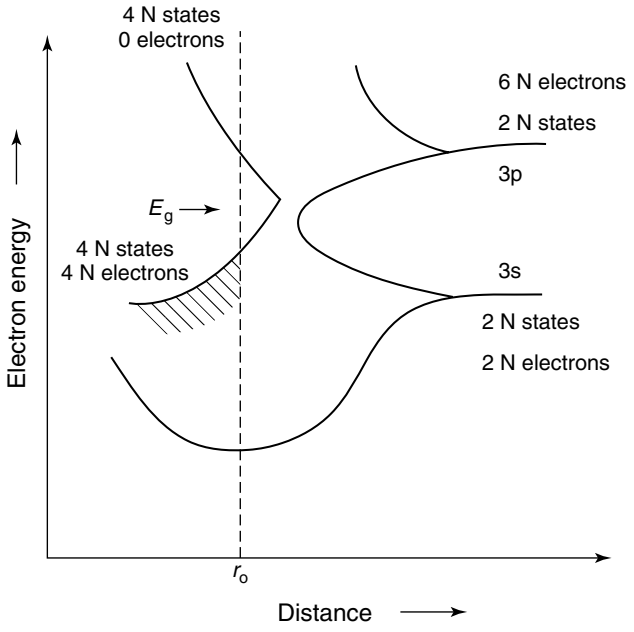

Fig. 1 Schematic illustration of how energy bands in semiconductors evolve from discrete atomic states for the specific example of silicon.

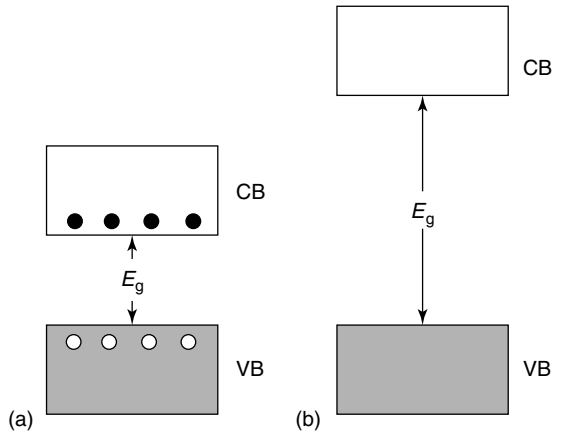

Fig. 2 Relative disposition of the CB and VB for a semiconductor (a) and an insulator (b). E_g is the optical band gap energy.

as the energy at which the probability of finding an electron is 1/2) can be regarded as the electrochemical potential of the electron in a particular phase (in this case, a solid). Thus, all electronic energy levels below E_F are occupied and those above E_F are likely to be empty.

Electrons in semiconductors may be regarded as low-density particle ensembles such that their occupancy in the valence and CBs may be *approximated* by the

Boltzmann function [14, 15]:

$$n_e \approx N_o \exp\left[-\frac{E_o - E_F}{kT}\right] \qquad (1)$$

Now we come to another important distinction between metals and semiconductors in that two types of electronic carriers are possible in the latter. Consider the thermal excitation of an electron from VB to CB. This gives rise to a free electron in the CB and a vacancy or hole in the VB. A localized chemical picture for the case of Si shows that the hole may be regarded as a missing electron in a chemical bond (Fig. 3). There is a crude chemical analogy here with the dissociation of a solvent such as water into H_3O^+ and OH^-. In either case, equal numbers of oppositely charged species are produced. Thus, Eq. (1) becomes:

$$n_i \approx N_c \exp\left[-\frac{E_F - E_c}{kT}\right] \qquad (2)$$

$$p_i \approx N_v \exp\left[-\frac{E_v - E_F}{kT}\right] \qquad (3)$$

In Eqs. (2–3), N_c and N_v are the effective density of states (in cm^{-3}) at the lower edge and top edge of CB and VB, respectively. These expressions can be combined with the recognition that $n_i = p_i$ to yield

$$n_i^2 \approx N_o \exp\left[-\frac{E_c - E_v}{kT}\right]$$

$$\approx N_o \exp\left[-\frac{E_g}{kT}\right] \qquad (4)$$

To provide a numerical sense of the situation, N_c and N_v are typically both approximately 10^{19} cm^{-3} so that the constant N_o ($N_c N_v$) in Eq. (1) is about 10^{38} cm^{-3}. For a semiconductor such as Si (with $E_g = 1.11$ eV, Table 1), n_i will be about 10^{10} cm^{-3} at 300 K according to Eq. (4). This rough calculation lends credence to the original rationale for the use of Boltzmann statistics for the electron energy distribution in semiconductors (see preceding section).

The preceding case refers to the semiconductor in its intrinsic state with very low carrier concentrations under ambient conditions. The Fermi level, E_F, in this case lies approximately in the middle of the energy band gap (Fig. 4a). This simply reflects the fact that the probability of electron occupancy is very high in VB and very low in CB and does not imply an occupiable energy level at E_F itself.

In extrinsic semiconductors the carrier concentrations are perturbed such that $n = p$. Again the analogy with the addition of an acid or base to water is quite instructive here. Consider the case when donor impurities are added to a neutral semiconductor. Since the intrinsic carrier concentrations are so low (sub-parts per trillion), even additions in parts per billion levels can have a profound electrical effect. This process is known as doping of the semiconductor. In this particular case, the Fermi level shifts toward the CB edge (Fig. 4b). When the donor level is

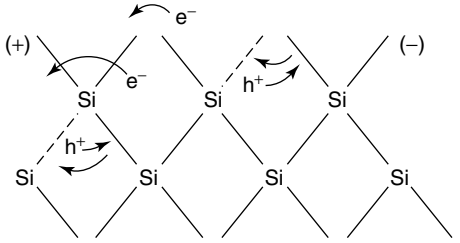

Fig. 3 A localized picture of electron-hole pair generation (see also Fig. 2a) in silicon.

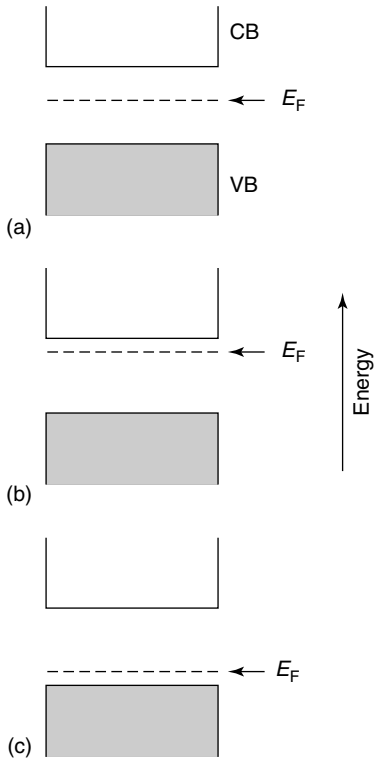

Fig. 4 Relative disposition of the Fermi level (E_F) for an intrinsic semiconductor (a), for an *n*-type semiconductor (b), and a *p*-type semiconductor (c).

within a few kT in energy from the CB edge, appreciable electron concentrations are generated by the donor ionization process (at ambient temperatures) such that now $n \gg p$. This is termed *n*-type doping, and the resultant (extrinsic) semiconductor is termed *n*-type. By analogy, *p*-type semiconductors have $p \gg n$. The terms minority and majority carriers now become appropriate in these cases. For a *p*-doped semiconductor case, the Fermi level now lies close to the VB edge (Fig. 4c). The movement of E_F with dopant concentration can also be rationalized via the Nernst formalism [6].

Doping can be accomplished by adding altervalent impurities to the intrinsic semiconductor. For example, P (a Group 15 or VA element) will act as a donor in Si (a Group 14 or IVA element). This can be rationalized on chemical terms by noting that P needs only four valence electrons for tetrahedral bonding (as in the Si lattice) – the fifth electron is available for donation by each P atom. The donor density, N_D nominally is approximately 10^{17} cm^{-3}. Thus, assuming that $n \simeq N_D$ (complete ionization at 300 K), p will be only approximately 10^3 cm^{-3} [recall that the product $n_i p_i$ is $\sim 10^{20}$ cm^{-6} (see preceding section)], bearing out the earlier qualitative assertion that $n \gg p$.

Impurity addition, however, is not the only doping mechanism. Nonstoichiometry in compound semiconductors such as CdTe (Table 1) also gives rise to *n*- or *p*-type behavior, depending on whether Cd or Te is in slight excess, respectively. The defect chemistry in these solid chalcogenides controls their conductivity and doping in a complex manner, a discussion of which is beyond the scope of this section. Excellent treatises are available on this topic and on the solid-state chemistry of semiconductors in general [16–22].

The foregoing discussion strictly refers to semiconductors in single-crystal form. Amorphous and polycrystalline counterparts present other complications caused by the presence of defects, trap states, grain boundaries, and the like. For this reason we orient the subsequent discussion mainly toward single crystals, although comparisons with less ideal cases are made where appropriate. The distinction between metal and semiconductor electrodes is important when we consider the electrostatics across the corresponding solid–liquid interfaces; this distinction is made in the following section.

1.3 The Semiconductor–Electrolyte Interface at Equilibrium

1.3.1 The Equilibration Process

The electrochemical potential of electrons in a redox electrolyte is given by the Nernst expression

$$E_{\mathrm{redox}} = E^{\mathrm{o}}{}_{\mathrm{redox}} + \frac{RT}{nF} \ln \left[\frac{c_{\mathrm{ox}}}{c_{\mathrm{red}}} \right] \qquad (5)$$

In Eq. (5), c_{ox} and c_{red} are the concentrations (roughly activities) of the oxidized and reduced species, respectively, in the redox couple. The parameter ($E_{\mathrm{redox}} = \mu_{\mathrm{e,redox}}$) as defined by Eq. (5) can be identified with the Fermi level ($E_{\mathrm{F,redox}}$) in the electrolyte. This was the topic of debate some years back [23], although this premise now appears to be well founded. The task now is to relate the electron energy levels in the solid and liquid phases on a common basis.

The semiconductor solid-state physics community has adopted the electron energy in vacuum as reference, whereas electrochemists have traditionally used the standard hydrogen electrode (SHE) scale. While estimates vary [23–25], SHE appears to lie at −4.5 eV with respect to the vacuum level. We are now in a position to relate the redox potential E_{redox} (as defined with reference to SHE) with the Fermi level $E_{\mathrm{F,redox}}$ expressed versus the vacuum reference (Fig. 5a)

$$E_{\mathrm{F,redox}} = -4.5 \text{ eV} - \mathrm{e_o} E_{\mathrm{redox}} \qquad (6)$$

When a semiconductor is immersed in this redox electrolyte, the electrochemical potential (Fermi level) is disparate across the interface. Equilibration of this interface thus necessitates the flow of charge from one phase to the other and a "band bending" ensues within the semiconductor phase. The situation before and after contact of the two phases is illustrated in Fig. 5(b) and (c) for an *n*-type and *p*-type semiconductor, respectively. After contact, the net result of equilibration is that $E_{\mathrm{F}} = E_{\mathrm{F,redox}}$ and a "built-in" voltage, V_{SC} develops within the semiconductor phase, as illustrated in the right hand frames of Fig. 5(b) and (c).

It is instructive to further examine this equilibration process. Consider again an *n*-type semiconductor for illustrative purposes (Fig. 5b). The electronic charge needed for Fermi level equilibration in the semiconductor phase originates from the donor impurities (rather than from bonding electrons in the semiconductor lattice). Thus, the depletion layer that arises as a consequence within the semiconductor contains positive charges from these ionized donors. The Fermi level in the semiconductor ($E_{\mathrm{F,n}}$) moves "down" and the process stops when the Fermi level is the same on either side of the interface. The rather substantial difference in the density of states on either side dictates that $E_{\mathrm{F,n}}$ moves farther than the corresponding level, $E_{\mathrm{F,redox}}$ in the electrolyte. A particularly lucid account of this initial charge transfer is contained in Ref. 6.

The band-bending phenomenon, shown in Fig. 5(b) and (c), is by no means unique to the semiconductor–electrolyte interface. Analogous electrostatic adjustments occur whenever two dissimilar phases are in contact (e.g. semiconductor-gas, semiconductor–metal). An important point of distinction from the corresponding metal case now becomes apparent. For a metal, the charge, and thus the associated potential drop, is concentrated at the surface penetrating at most a few Å into the interior. Stated differently, the high electronic conductivity of a metal cannot support an electric field

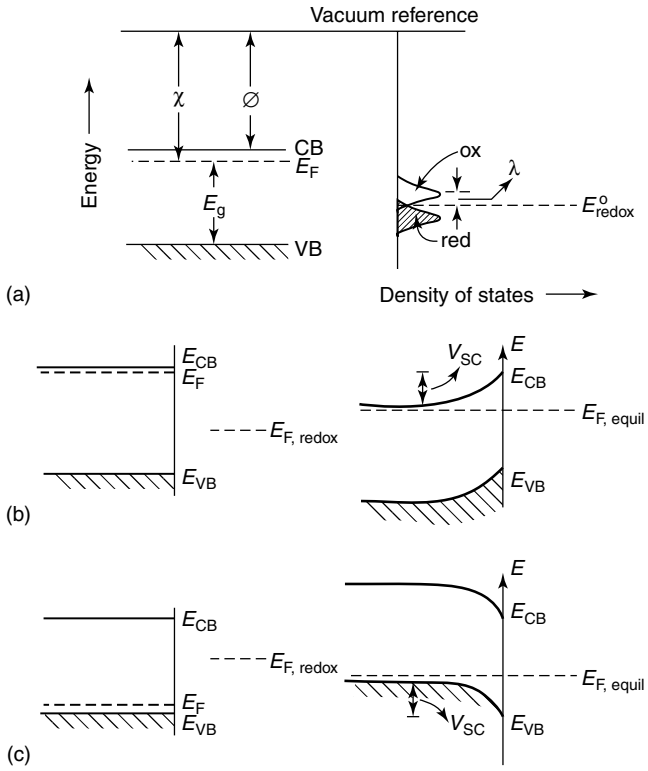

Fig. 5 (a) Energy levels in a semiconductor (left-hand side) and a redox electrolyte (right-hand side) shown on a common vacuum reference scale. χ and ϕ are the semiconductor electron affinity and work function, respectively. (b) The semiconductor-electrolyte interface before (LHS) and after (RHS) equilibration (i.e. contact of the two phases) shown for a *n*-type semiconductor. (c) As in (b) but for a *p*-type semiconductor.

within it. Thus, when a metal electrode comes into contact with an electrolyte, almost all the potential drop at the interface occurs within the Helmholtz region in the electrolyte phase. On the other hand, the interfacial potential drop across a semiconductor-electrolyte junction (see following) is partitioned both as V_{SC} and as V_H leading to a simple equivalent circuit model comprising two capacitors (C_{SC} and C_H) in series (Fig. 6). Further refinements of the equivalent circuit description are given later but the point to note is the rather variant behavior of a metal and a semiconductor at equilibrium with a redox electrolyte.

1.3.2 The Depletion Layer

There is a characteristic region within the semiconductor within which the charge would have been removed by the equilibration process. Beyond this boundary, the ionized donors (for a *n*-type semiconductor), have their compensating

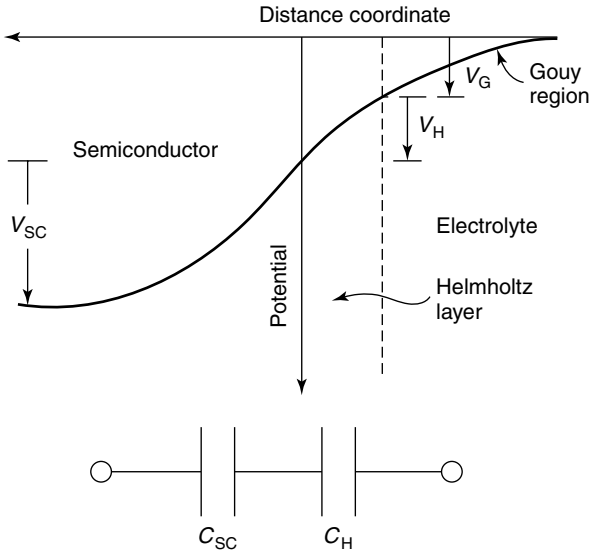

Fig. 6 Electrostatics at a semiconductor–electrolyte interface. A highly simplified equivalent circuit for the interface at equilibrium is shown at the bottom. The Gouy layer is neglected in the latter case (see text).

charge (electrons), and the semiconductor as a whole is electrically neutral. This layer is the space charge region or the depletion layer, so termed because the layer is depleted of the majority carriers. The potential distribution in this interfacial region can be quantified by relating the charge density and the electric field strength as embodied by the Poisson equation [14, 26]. Under restrictive conditions, more fully discussed in Refs. 6 and 14, we obtain a particularly simple expression

$$V(x) = -\left(\frac{e_o N_D}{2\varepsilon_s}\right) x^2 \times (o \le x \le W) \qquad (7)$$

In Eq. (7), e_o is the electronic charge and ε_s is the static dielectric constant of the semiconductor. The potential distribution is mapped in Fig. 6. We are now in a position to quantify the parameter V_{SC}:

$$V_{SC} = -\left(\frac{e_o N_D}{2\varepsilon_s}\right) W^2 \qquad (8)$$

where W is the depletion layer width.

Further reflection shows how the magnitude of W should depend on the semiconductor parameter N_D. Consider two cases of a semiconductor, one that is lightly doped (say $N_D \sim 10^{16}$ cm^{-3}) and another that is heavily doped ($N_D \sim 10^{18}$ cm^{-3}). Obviously in the former case, the charge needed for Fermi level equilibration has to come from deeper into the solid and so the magnitude of W will be larger. This suggests a strategy for chemical control of the electrostatics at the semiconductor–electrolyte interface [6]. Nominal dimensions of W are in the 10–1000 nm range. This may be compared with the corresponding Helmholtz layer width, typically 0.4–0.6 nm. With the capacitor-in-series model (see earlier section), we can see that the semiconductor space charge

layer is usually the determinant factor in the total capacity of the interface. Once again, the contrast with the corresponding metal–electrolyte interface is striking. Only when the semiconductor is degenerately doped (leading to rather large space charge layer charge, Q_{SC} and "thin" depletion layer widths) or when its surface is in accumulation does the situation become akin to the metal–electrolyte interface (see following).

1.3.3 Mapping of the Semiconductor Band-edge Positions Relative to Solution Redox Levels

Considerations of interfacial electron transfer require knowledge of the relative positions of the participating energy levels in the two (semiconductor and solution) phases. Models for redox energy levels in solution have been exhaustively treated elsewhere [27, 28]. Besides the Fermi level of the redox system (Eq. 6), the thermal fluctuation model [27, 28] leads to a Gaussian distribution of the energy levels for the occupied (reduced species) and the empty (oxidized species) states, respectively, as illustrated in Fig. 5(a). The distribution functions for the states are given by

$$D_{ox} = \exp\left[-\frac{E - E_{F,redox} - \lambda^2}{4\,kT\,\lambda}\right] \quad (9a)$$

$$D_{red} = \exp\left[-\frac{E - E_{F,redox} + \lambda^2}{4\,kT\,\lambda}\right] \quad (9b)$$

In Eqs. (9a) and (9b), λ is the solvent reorganization energy.

Now consider the relative disposition of these solution energy levels with respect to the semiconductor band edge positions at the interface. The total potential difference across this interface (Fig. 6) is given by

$$V_t = V_{SC} + V_H + V_G \quad (10)$$

In Eq. (10), V_t is the potential as measured between an ohmic contact on the rear surface of the semiconductor electrode and the reference electrode (Fig. 6). The problematic factors in placing the semiconductor and solution energy levels on a common basis involve V_H and V_G. In other words, theoretical predictions of the magnitude of V_{SC} (and how it changes as the redox couple is varied) are hampered by the lack of knowledge on the magnitude of V_H and V_G. A degree of simplification is afforded by employing relatively concentrated electrolytes such that V_G can be ignored.

As with metals, the Helmholtz layer is developed by adsorption of ions or molecules on the semiconductor surface, by oriented dipoles, or especially in the case of oxides, by the formation of surface bonds between the solid surface and species in solution. Recourse to band edge placement can be sought through differential capacitance measurements on the semiconductor–redox electrolyte interface [29].

In the simplest case as more fully discussed elsewhere [14, 15, 29], one obtains the Mott-Schottky relation (for the specific instance of a *n*-type semiconductor) of the semiconductor depletion layer capacitance (C_{SC}), again by invoking the Poisson equation

$$1/C_{SC}^2 = \frac{2}{N_D e_o \varepsilon_s}\left[(V - V_{fb}) - \frac{kT}{e_o}\right] \quad (11)$$

In Eq. (11), V_{fb} is the so-called flat band potential, that is the applied potential (V) at which the semiconductor energy bands are "flat", leading up to the solution junction. Several points with respect to the applicability of Eq. (11) must be noted.

The Mott-Schottky regime spans about 1 V in applied bias potential for most semiconductor–electrolyte interfaces (i.e.

in the region of depletion layer formation of the semiconductor space charge layer, see preceding section) [15]. The simple case considered here involves no mediator trap states or surface states at the interface such that the equivalent circuit of the interface essentially collapses to its most rudimentary form of C_{SC} in series with the bulk resistance of the semiconductor. Further, in all the earlier discussions, it is reiterated that the redox electrolyte is sufficiently concentrated that the potential drop across the Gouy (diffuse) layer in the solution can be neglected. Specific adsorption and other processes at the semiconductor–electrolyte interface will influence V_{fb}; these are discussed elsewhere [29, 30] as are anomalies related to the measurement process itself [31]. Figure 7 contains representative Mott-Schottky plots for both *n*- and *p*-type GaAs electrodes in an ambient temperature molten salt electrolyte [32].

Once V_{fb} is known (from measurements), the Fermi level of the semiconductor at the surface is defined. It is then a simple matter to place the energies corresponding to the conduction and VBs at the surface (E_{CB} and E_{VB}, respectively) if the relevant doping levels are known. The difference between E_{CB} and E_{VB} should approximately correspond to the semiconductor band gap energy, E_g (see Figs. 4 and 7). Alternatively, if V_{fb} is measured for one given state of doping of the semiconductor (*n*- or *p*-doped), the other band edge position can be fixed from

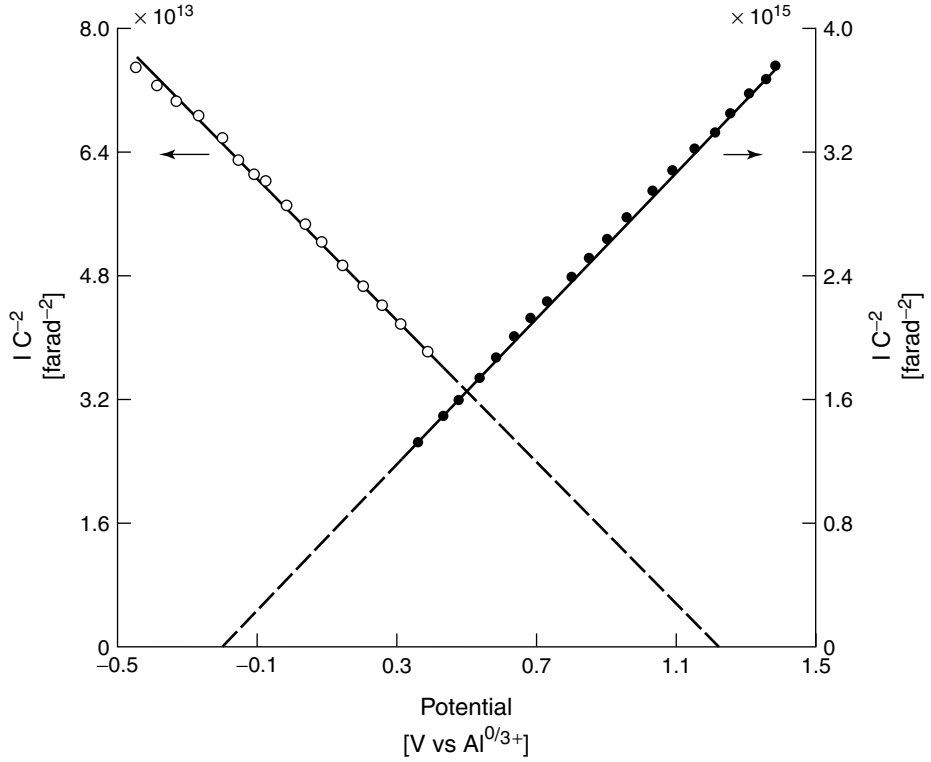

Fig. 7 Mott-Schottky plots for *n*- and *p*-type GaAs electrodes in an $AlCl_3$/*n*-butylpyridinium chloride molten-salt electrolyte. (Reproduced with permission from Ref. 32.)

knowledge of E_g. It is important to stress that the semiconductor surface band edge positions (as estimated from V_{fb} measurements) comprises all the terms in Eq. (10) and reflects the situation in situ for a given set of conditions (solution pH, redox concentration, etc.) of the semiconductor-redox electrolyte. The situation obviously becomes complex when the charge distribution and mediation at the interface changes either via surface states and illumination or both. These complications are considered later. Figure 8 contains the relative dispositions of the surface band edges mapped for a number of semiconductors in aqueous media.

Having located the semiconductor band edge positions (relative either to the vacuum reference or a standard reference electrode), we can also place the Fermi level of the redox system, $E_{F,redox}$, on the same diagram. Energy diagrams such as those in Fig. 8 are important in considerations of charge transfer as we shall see later. In anticipation of this discussion, it is apparent that the three situations illustrated in Fig. 9 for an *n*-type semiconductor–electrolyte interface entail the participation of the semiconductor CB, VB, and even states in its band gap in charge exchange with the solution species. Here again is a point of departure from the metal case; viz., for a semiconductor, hole, electron, and surface state pathways must all be considered.

Let us return to the band bending process at the interface. For a given semiconductor, the expectation is that as the redox Fermi level is moved more positive (''down'' on the energy diagram),

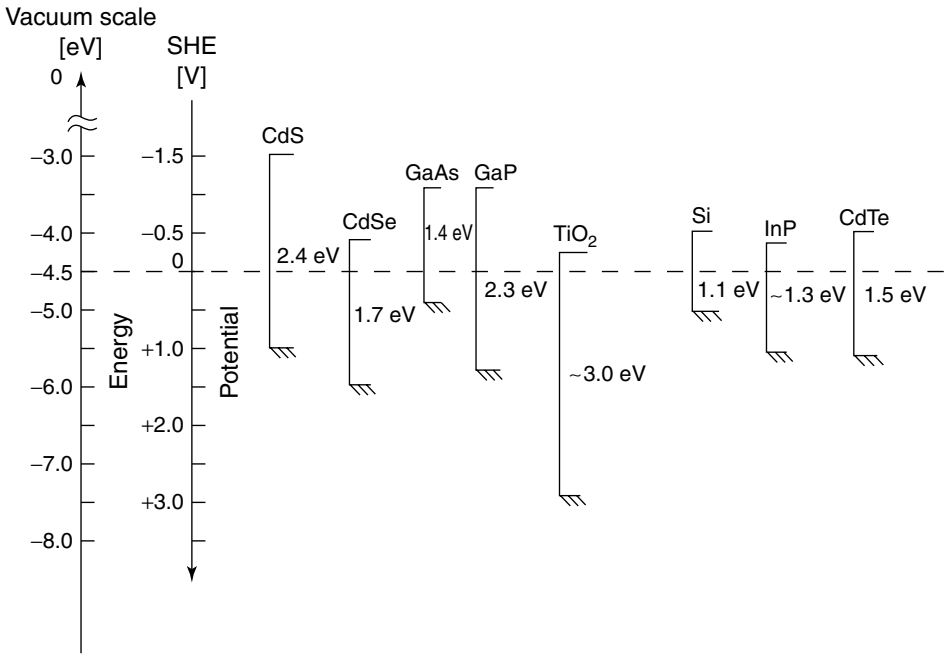

Fig. 8 Relative dispositions of various semiconductor band edge positions shown both on the vacuum scale and with respect to the SHE reference. These band edge positions are for an aqueous medium of pH ~1.

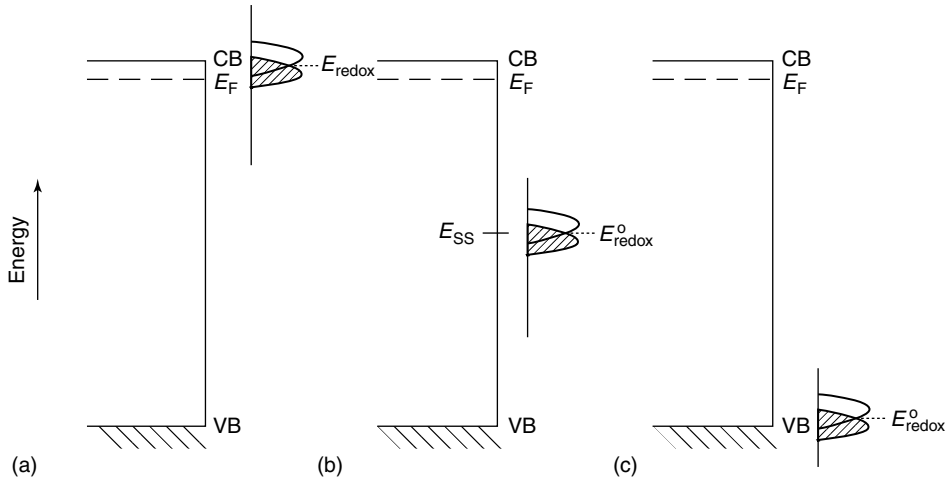

Fig. 9 Three situations for a *n*-type semiconductor–electrolyte interface at equilibrium showing overlap of the redox energy levels with the semiconductor CB (a), with surface states (b), and with the semiconductor VB (c). A discrete energy level is assumed for the surface states as a first approximation.

V_{SC} should increase concomitantly. This is the ideal (band edge "pinned") situation. In other words [23]

$$\frac{d\Delta V_{SC}}{dE_{redox}} = 1 \qquad (12)$$

Equation (12) reflects the fact that the change in band bending faithfully tracks the redox potential change. A measure of the former is the open-circuit photopotential (see following). Figure 10 shows that this ideal situation indeed is realized for selected semiconductor–electrolyte interfaces [33]. As further discussed later, the analogy with the corresponding metal-semiconductor junctions (Schottky barriers) is direct [5, 34–36].

Complications arise when there are surface states that mediate charge exchange at the interface. When their density is

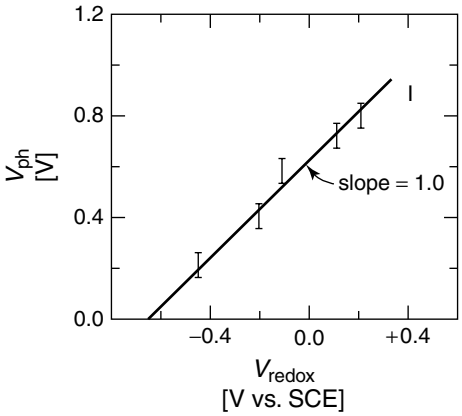

Fig. 10 Plot of the open-circuit photovoltage for amorphous Si-methanol interfaces containing a series of one-electron redox couples. (Reproduced with permission from Ref. 33.)

high [37], they act as a "buffer", in that in the extreme case, carriers in the semiconductor energy bands are completely excluded from the equilibration process.

1.3.4 Surface States and Other Complications

Surface states arise because of the abrupt termination of the crystal lattice at the surface; obviously the bonding arrangement is different from that in the bulk. Consider our prototype semiconductor, Si. The tetrahedral bonding characteristic of the bulk gives way to coordinative unsaturation of the bonds for the Si surface atoms. This unsaturation is relieved either by surface reconstruction or bonds with extraneous (e.g. solvent) species [29, 38–40]. The surface bonding results in a localized electronic structure for the surface that is different from the bulk. The energies of these localized surface orbitals nominally lie in the forbidden band gap region. The corresponding states are thus able (depending on their energy location) to exchange charge with the conduction or VBs of the semiconductor and/or the redox electrolyte [29].

Unlike the case illustrated in Fig. 10, changes in the solution redox potential have been observed to cause no change in the magnitude of V_{SC}. This situation is termed Fermi level pinning; in other words, the band edge positions are unpinned in these cases so that the movement of E_{redox} is accommodated by V_H rather than by V_{SC}. As mentioned earlier, it appears [37] that surface state densities as low as $10^{13}\,cm^{-2}$ (~1% of a monolayer) suffice to induce complete Fermi level pinning in certain cases. Of course, intermediate situations are possible. Thus, the ideal case manifests a slope of 1 in a plot of V_{SC} (or an equivalent parameter) versus E_{redox} (see Fig. 10). On the other hand, complete pinning results in a slope of zero. Intermediate cases of Fermi level exhibit slopes between 0 and 1 [41]. As stated earlier, there is a direct analogy here with the metal/semiconductor junction counterparts [42, 43]:

$$\phi_B = S\phi_m + \text{const} \qquad (13)$$

In Eq. (13), ϕ_B is the so-called Schottky barrier height, ϕ_m is the metal work function, and S is a dimensionless parameter. Attempts have been made to relate S to semiconductor properties [44–48].

To further complicate matters, the nonideal behavior of semiconductor–electrolyte interfaces as noted earlier is exacerbated when the latter are irradiated. Changes in the occupancy of these states cause further changes in V_H, so that the semiconductor surface band edge positions are different in the dark and under illumination. These complications are considered later. The surface states as considered earlier are shallow (with respect to the band edge positions) and can essentially be considered as completely ionized at room temperature. However, for many oxide semiconductors, the trap states may be deep and thus are only partially ionized. Specifically, they may be disposed with respect to the semiconductor Fermi level such that they are ionized only to a depth that is small relative to W [49]. The physical manifestation of such deep traps as observed in the AC impedance behavior of semiconductor–electrolyte interfaces has been discussed [14, 49].

Finally, within the Mott-Schottky approximation (Eq. 11), large values of ε_s or N_D can lead to the ratio V_H/V_{SC} becoming significant. Figure 11 contains estimates of this ratio for several values of N_D for a semiconductor with a large ε_s value (TiO_2, $\varepsilon_s = 173$) mapped as a function of the total

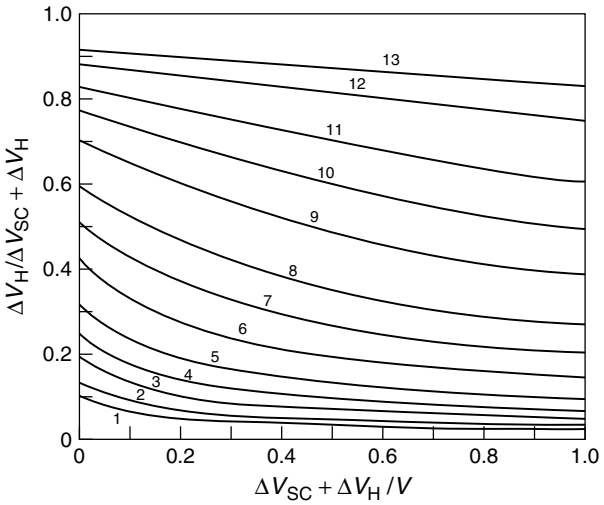

Fig. 11 The ratio of the potential drop in the Helmholtz to the total potential change computed as a function of the total potential change. A static dielectric constant of 173 (typical of TiO_2) and a Helmholtz capacitance of 10 μF/cm^2 were assumed and the doping density was allowed to vary from 10^{16} cm^{-3} (curve 1) to 10^{20} cm^{-3} (curve 13). (Reproduced with permission from Ref. 50.)

potential drop across the interface [50]. Clearly V_H can become a sizable fraction of the total potential drop (approaching the situation for metals) under certain conditions. It has been shown [51] that the Mott-Schottky plots will still be linear but the intercept on the potential axis is shifted from the V_{fb} value.

1.4 Charge Transfer Processes in the Dark

1.4.1 Current-potential Behavior

Let us return to the equilibrium situation of an *n*-type semiconductor in contact with a redox electrolyte and reconsider the situation in Fig. 9(a). This is shown again in Fig. 12(a) to underscore the fact that the interface is in a state of *dynamic* equilibrium. That is, the forward and reverse (partial) currents exactly balance each other and there is no *net* current flow across the interface. In fact, the situation here is similar to that occurring for a metal–redox electrolyte interface at the rest potential. We can write down expressions for the net current using a kinetics methodology as in Ref. 6 with some minor changes in notation:

$$i_c = -e_o A k_{et} c_{ox} (n_s - n_{so}) \qquad (14)$$

In Eq. (14), k_{et} is the rate constant for electron transfer, c_{ox} is the concentration of empty (acceptor) state in the redox electrolyte, n_s and n_{so} are the surface concentrations of electrons, the subscript "o" in the latter case denoting the equilibrium situation. Thus, as long as the semiconductor–electrolyte interface is not perturbed by an external (bias) potential, $n_s \equiv n_{so}$ and the net current is zero. The voltage

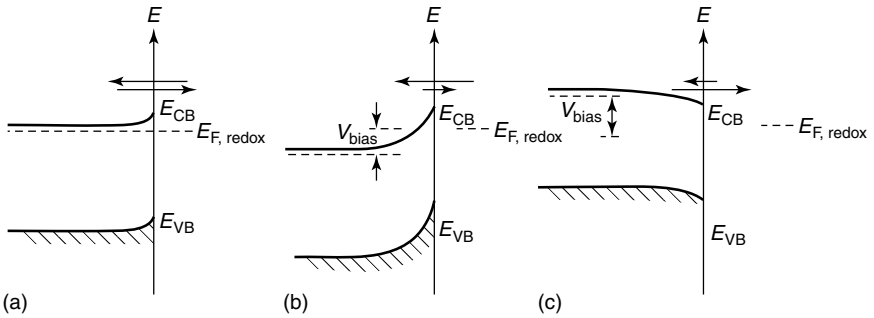

Fig. 12 Three situations for a *n*-type semiconductor–electrolyte interface at equilibrium (a), under reverse bias (b), and under forward bias (c). The size of the arrows denotes the magnitudes of the current in the two (i.e. anodic and cathodic) directions.

dependence of the current is embodied in the ratio, n_s/n_{so}, which can be regarded as a measure of the extent to which the interface is driven away from equilibrium. It must be noted that n_{so} is *not* the bulk concentration of majority carriers (n) in the semiconductor because of the potential drop across the space charge layer [6, 35].

$$n_{so} = n \exp\left(-\frac{e_o V_{SC}}{kT}\right) \qquad (15)$$

A few words about the units of the terms in Eq. (14) are in order at this juncture. The term $i/e_o A$ may be regarded as a flux (J) in units of number of carriers crossing per unit area per second [1, 3, 8]. The concentration terms are in cm^{-3}; thus k_{et} has the dimensions of $cm^4 s^{-1}$ because of the second-order kinetics nature stemming from the two multiplied concentration terms in Eq. (14) [1, 3, 8].

Consider now the application of a bias potential to the interface. Intuitively when it is such that $n_s > n_{so}$, a reduction current (cathodic current) should flow across the interface such that the oxidized redox species are converted to reduced species (Ox $\rightarrow$ Red). On the other hand, when $n_{so} > n_s$, the current flow direction is reversed and an anodic current should flow. Once again the situation here is somewhat similar to the metal case. The major difference resides in the vastly different state densities in the solid and the existence of an energy gap region. The two nonequilibrium situations are shown in Figs. 12(b) and 12(c), respectively. Away from equilibrium, we have the analogous Boltzmann expression counterpart to Eq. (15)

$$n_s = n \exp\left[-\frac{e_o(V_{SC} + V)}{kT}\right] \qquad (16)$$

leading, in turn, to

$$i_c = -e_o A k_{et} c_{ox} n_{so} \times \left[\exp\left(-\frac{e_o V}{kT}\right) - 1\right] \qquad (17)$$

The assumption is inherent in the preceding discussion that *all* of the applied bias (V) drops across the space charge layer such that we are modulating only the majority carrier population at the surface (and not the potential drop across the Helmholtz layer). In other words, the band edge positions are pinned or there is no Fermi level pinning (see Sect. 1.3.4).

Analogous expressions may be developed for majority carrier flow for a *p*-type semiconductor in contact with a redox electrolyte, with the important caveat that the VB is involved in this process instead.

Equation (17) suggests that the cathodic current is exponentially dependent on potential for $V < 0$. This is the so-called forward-bias regime. On the other hand, when $V > 0$ (reverse-bias regime) the current is essentially independent of potential and, importantly, is of opposite sign. Simply put, in this case, the electron flow direction (i.e. anodic) is from the occupied redox states into the semiconductor CB (Fig. 12c). It should not, thus, be surprising that this process is independent of potential. Both bias regimes are contained in curve 1 in Fig. 13.

Of particular interest to this discussion is the ''preexponential'' term in Eq. (17):

$$i_o = e_o A k_{et} c_{ox} n_{so} \qquad (18)$$

Analogous to the metal case, we can call this term the exchange current; it is the current that flows at equilibrium when the partial cathodic and anodic components exactly balance one another. Of particular interest is the dependence of i_o on n_{so}. Also, variations in c_{ox} will affect the magnitude of i_o. Both these trends can be readily rationalized. Finally, i_o will increase with doping because of the ''thinness'' of the resultant barrier at the surface.

When $E_{F,redox}$ is moved ''down,'' that is more positive, the band bending increases, V_{SC} increases and thus n_{so} decreases. A similar alteration in c_{ox} affects $E_{F,redox}$ through the Nernst expression. In both instances, we are influencing the Fermi level at the interface at equilibrium. Thus, in a sense, i_o is a quantitative measure of the extent of rectification of a given interface; that is, a smaller i_o value translates to better rectification.

The reverse bias current remains at a very low value because of the lack of minority carriers (i.e. holes for n-type semiconductor) in the dark. Alternatively, injection of electrons from occupied redox levels (also an anodic current) has to thermally surmount the surface barrier [5, 34, 35]. Under extreme reverse bias, however, this barrier becomes ''thin'' and electrons can tunnel through it, leading to an abrupt increase in the anodic current. This process was studied even in the early days of

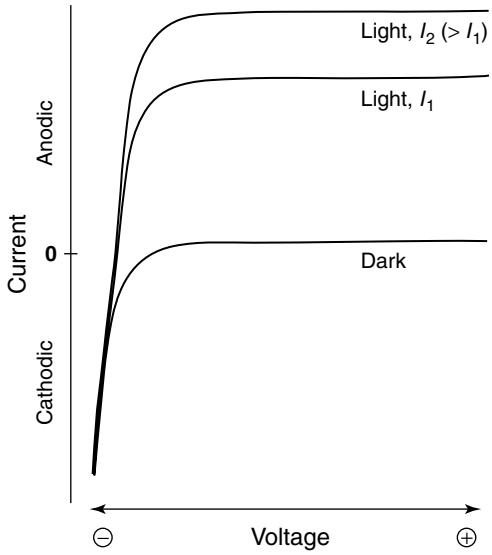

Fig. 13 Current-potential curves for a n-type semiconductor in the dark (curve 1) and under band gap illumination (curves 2 and 3). Two levels of photon fluxes are shown in the latter case.

semiconductor electrochemistry [52] and a detailed discussion is found in a book chapter [14]. Ultimately the junction "breaks down" (at the so-called Zener limit). This dark current flow is not shown in Fig. 13 (curve 1).

Returning to the forward-bias (cathodic) current flow, Eq. (17) bears some analogy to the famous Tafel expressions in electrochemical kinetics. Thus, ignoring the unity term within the square brackets, Eq. (17) predicts a Tafel slope of 60 mV per decade at 298 K. In many instances [53, 54], such a slope indeed is observed. In many cases, however, the slopes are higher than the "ideal" value [14, 55–59].

The causes for this anomalous behavior are still not fully understood. It appears likely that many factors are involved: surface film formation, varying potential drop across the Helmholtz region caused, for example, by surface state charging, and so on. Even crystallographic orientations appear to be important [59]. These aspects have been discussed by other authors [14, 55, 60].

We have so far considered only (majority carrier) processes involving the CB (again assuming for illustrative purposes a *n*-type semiconductor). Consider the interfacial situation depicted in Fig. 9(c). The energy states of the redox system now overlap with the VB of the semiconductor such that *hole injection* in the "dark" is possible. When the band bending is large, the injected holes remain at the surface and attack the semiconductor itself, causing the latter to undergo corrosion. If the bias potential is such that the band bending is modest and the holes recombine with electrons (either via the surface states or in the space charge region itself), a cathodic current flows that is carried by the majority carriers in the bulk. This recombination current pathway is schematized in Fig. 14 and is further discussed in the next section. Hole injection has been extensively studied especially for III–V (Group 13–15) semiconductors such as GaAs and GaP because of the relevance of this process to electroless etching and device fabrication technology. This topic has been reviewed [61–64].

The invokement of either the CB or the VB of the semiconductor in charge exchange in the dark with solution redox species is not always straightforward. This is particularly true for multielectron redox processes to be discussed later. Movement of the semiconductor band edge positions (i.e. band edge unpinning) relative to the redox energy levels also presents a complicating situation (see following). Some cases (e.g. $Eu^{2+/3+}$ in contact with GaAs electrodes) are interesting in that the same

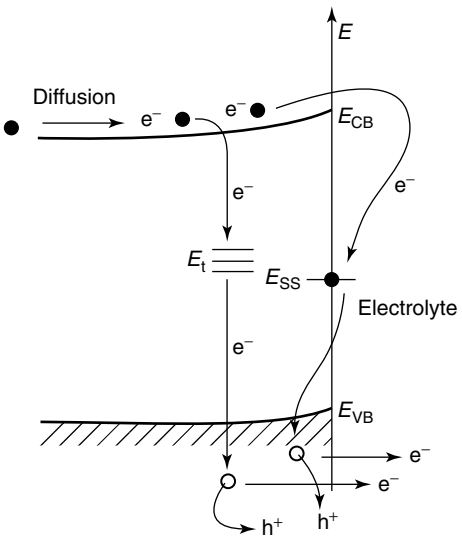

Fig. 14 Hole injection into the VB of a *n*-type semiconductor from an oxidant (e.g. Fe^{3+}) and the injection or recombination pathway. Both surface state–mediated and depletion layer trap–mediated routes are shown for the recombination.

couple can interact with both bands [55, 65]. Thus, the oxidation of Eu^{2+} is a VB process (occurring at *p*-GaAs but not at *n*-GaAs in the dark), whereas the reduction of Eu^{3+} (a facile process that reportedly occurs at rates close to the thermionic emission limit, Ref. 55) is mediated by CB electrons [65]. The $[Cr(CN)_6]^{3-/4-}$ redox system behaves in a similar manner with respect to GaAs [66].

Electroluminescence, (EL), is a versatile probe for studying such carrier injection processes. Thus, hole injection into the VB of a *n*-type semiconductor leads to cathodic EL, whereas electron injection into the CB of a *p*-type semiconductor leads to anodic EL [67]. Examples of studies of cathodic EL are commonplace [68–70]; however, anodic EL is not very common because the energy requirement for the redox couple has a very negative redox potential. Nonetheless, anodic EL has been reported for the *p*-InP-$[Cr(CN)_6]^{4-}$ interface [71]. Radical intermediates can also cause EL as discussed later for multielectron redox processes. EL is treated in more depth in another chapter.

This finally brings us to the comparability of the current-potential behavior of *n*-type and *p*-type samples of a given semiconductor. It may be noted that for a redox process occurring via one of the bands (e.g. VB), the cathodic currents (electron transfer from VB to Ox) are expected to be equal for *n*- and *p*-type materials. This idea has been pursued using the so-called quasi-Fermi level concept [55, 72, 73]. This model has been demonstrated quantitatively by studying the anodic decomposition of GaAs and the oxidation of redox species such as Cu^{+} and Fe^{2+} at *n*- and *p*-type GaAs electrodes [72, 73].

1.4.2 Dark Processes Mediated by Surface States or by Space Charge Layer Recombination

Surface states were considered earlier (Sect. 1.3.4) from an electrostatic perspective. Here we examine their dynamic consequences. There are two principal charge transfer routes involving surface states. Consider again an *n*-type semiconductor; the forward-bias current can either involve direct exchange of electrons between the semiconductor CB and Ox states in solution (Fig. 12b) or can be mediated by surface states (Fig. 15). The second

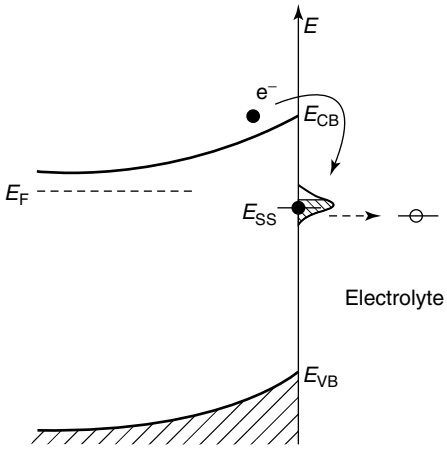

Fig. 15 Surface state–mediated electron injection from the CB of a *n*-type semiconductor into the electrolyte.

route involves hole injection into the semiconductor VB again from Ox states in solution (Figs. 9c and 14). The recombination current is mediated either by surface states or via space charge layer recombination. We will consider first the CB process.

Initial evidence for the intermediacy of surface states came from dark current measurements on n-TiO_2 and n-$SrTiO_3$ in the presence of oxidizing agents such as $[Fe(CN]_6{}^{3-}$, Fe^{3+}, and $[IrCl_6]^{2-}$ [74, 75]. Similar early evidence that the charge transfer process was more complex than direct transfer of electrons from the semiconductor CB also came from AC impedance spectroscopy measurements on n-ZnO, n-CdS, and n-CdSe in contact with $[Fe(CN)_6]^{3-}$ species [76, 77].

The electrochemical impedance for surface state–mediated charge transfer has been computed recently [78]. The key results are summarized in Fig. 16. Figure 16(a) contains the proposed equivalent circuit for the process and features a parallel connection of the impedance for the Faradaic process $[Z_F(\omega)]$ (ω = angular frequency, $2\pi f$) and the capacitance of the semiconductor depletion layer, C_{SC}. The

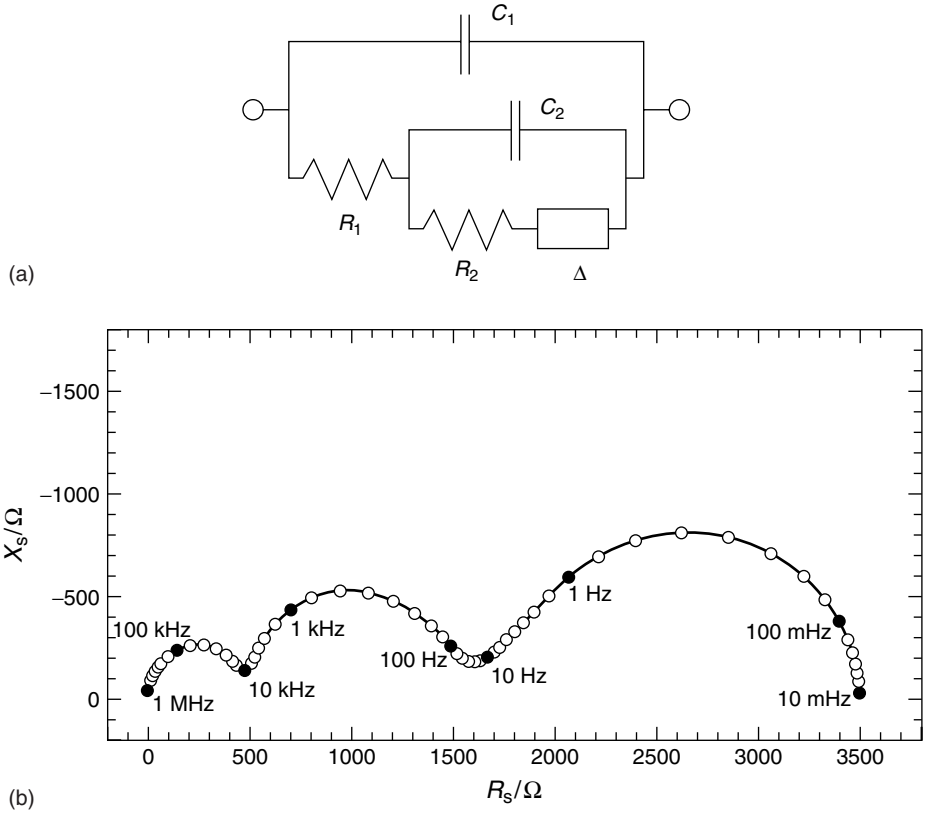

Fig. 16 Equivalent circuit (a) and a simulated Nyquist plot (b) for the charge-transfer pathway illustrated in Fig. 15. The capacitance C_1 represents that of the space charge layer and the parallel branch components represent the Faradaic charge-transfer process. Refer to the original work for further details. (Reproduced with permission from Ref. 78.)

former also involves a diffusion impedance (Δ) of the Warburg type (see following). The complex plane (Nyquist) plot predicted for the circuit is illustrated in Fig. 16(b). The theoretically predicted AC impedance response was compared with experiments on *n*-GaAs rotating disk electrodes in sulfuric acid media [79]. The equivalent circuit in Fig. 16(a) was also compared with previous versions proposed by other authors [80–83]. These alternate versions differ in their assumption of no variations in potential drop across the Helmholtz region (i.e. infinite C_H) and no concentration polarization in the electrolyte phase (infinite diffusion coefficient for the redox species). Also discussed is the application of AC impedance spectroscopy for studying the kinetic reversibility of majority carrier charge transfer via the CB of a *n*-type semiconductor [82].

AC impedance spectroscopy also has seen extensive utility in the study of the hole injection or recombination process depicted in Fig. 14. An equivalent circuit for this process is illustrated in Fig. 17; it does resemble the circuit in Fig. 16(a), except for the Warburg component [84]. Early studies [85–88] utilized the recombination resistance parameter, R_r, that was extracted from model fits of the measured AC impedance data. This parameter was seen to be inversely related to the hole injection current, thus signifying that it is indeed related to the recombination process. However, the challenge is to differentiate whether recombination is mediated via surface states or whether it occurs in the depletion layer. Thus, the parameter R_r alone cannot afford this information and both the real and the imaginary parts of this additional impedance must be considered. Subsequent studies have addressed this aspect [85, 89–93]. The admittance corresponding to recombination at the surface [92] and in the space charge layer [93] was calculated from first principles. These computations show that the recombination *capacitance* increases monotonically with decreasing band bending in the latter case, whereas it shows a peak in the former case as a function of potential.

Experimental studies [91] show that in the case of *n*-GaAs electrodes in contact with Ce^{4+} as the hole injection agent, surface recombination prevails. On the other hand, with *n*-GaP electrodes, recombination in the depletion layer must also be taken into account. Other discussions of the use of AC impedance spectroscopy for the study of hole injection or recombination are contained in Refs. 78 and 84.

The consequences of potential drop variations across the Helmholtz layer in the hole injection process have been examined by a variety of techniques [94, 95]. For example, chemical reaction of the GaAs surface with iodine results in a downward shift of the semiconductor band edge positions such that the reduction of iodine is mediated by CB electrons [95]. When sufficient negative charge accumulates at

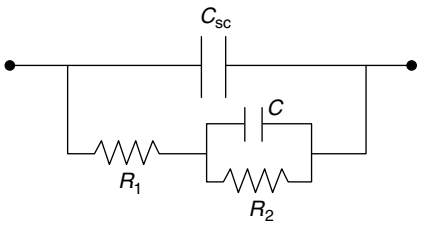

Fig. 17 Equivalent circuit representation of the injection or recombination process. (Reproduced with permission from Ref. 84.)

the surface, the potential is redistributed between the semiconductor spacecharge layer and the Helmholtz region. Now iodine is reduced by hole injection as gauged by EL and AC impedance measurements [95].

1.4.3 Rate-limiting Steps in Charge Transfer Processes in the Dark

The assumption is implicit in the discussion in Sect. 1.4.1 (leading to Eq. 18) that charge transfer kinetics at the semiconductor–electrolyte interface is the rate-limiting step. Fundamentally, we have to differentiate majority carrier *capture* and minority carrier *injection* processes in the dark. In the former case, transit through the semiconductor itself or charge exchange with the surface states can be potentially rate-limiting. In the latter case, there are three steps involved: hole injection into the semiconductor VB, charge exchange between the recombination center and the semiconductor CB, and diffusion of majority carriers (electrons) from the neutral region. Finally, mass transport processes in the electrolyte phase itself can be a limiting factor in the overall current flow. We shall examine carrier capture and injection processes in turn.

The vast majority of outer-sphere, nonadsorbing redox systems to date have yielded values for k_{et} in the $10^{-17} - 10^{-16}$ cm^4 s^{-1} range [3, 8]. These include n-Si-CH_3OH [96, 97], n-InP-CH_3OH [98], $GaInP_2$-coated n-GaAs-acetonitrile [99], and p-GaAs-HCl [100] interfaces. The redox couples in these studies have mostly involved metallocenes that show low proclivity to adsorb on the semiconductor surface. In these cases, the rate-determining step in the overall current flow undoubtedly lies in the electron transfer event at the interface itself. However, values for k_{et} approximately three orders of magnitude higher have also been reported for similar interfaces, namely, n-GaAs-acetonitrile-containing cobaltocenium [$Co(Cp)_2^+$] acceptors [99, 101]. Similarly, high values were reported for p-GaAs-acetonitrile interfaces with ferricenium and cobaltocenium redox species [102]. In these latter cases, alternative mechanisms (e.g. thermionic emission, see following) must be invoked in a rate-limiting role. Quartz crystal microbalance measurements have yielded evidence for adsorption of redox species (and consequently high *local* substrate concentration) in some of these "anomalous" instances [101].

In the majority carrier capture process, if the interfacial charge transfer kinetics are facile, the transport of majority carriers through the space charge region can play a rate-limiting role. The thermionic emission theory [34] assumes that every electron that reaches the semiconductor surface, and has the appropriate energy to overcome the potential barrier there, will cross the interface with a tunnel probability of unity. However, if the interfacial kinetics are sluggish, some of the electrons will be reflected at the interface. In this case, the exchange current i_o is no longer described by Eq. (18) but by Eq. (19) [34]

$$i_o = AA^* \left(\frac{m^*}{m_e}\right) T^2 \left(\frac{n_s}{n}\right) \qquad (19)$$

In Eq. (19), A is the electrode area, A^* is the Richardson constant (120 A K^{-2} cm^{-2}), m^*/m_e is the relative effective electron mass in the CB, and T is the absolute temperature.

In many of the reported instances [53, 55, 103], the current calculated from Eq. (19) is much higher than that measured experimentally, signaling that interfacial charge-transfer kinetics are limiting

the overall rate. On the other hand, in the *n*-GaAs-acetonitrile-$Co(Cp)_2^+$ case [101], AC impedance spectroscopy data appear to support the assumption that thermionic emission is the current-limiting transport mechanism.

Another factor that enters into this discussion is the mobility of the majority carriers. It has been argued [14] that in the case of low mobility materials (e.g. $\mu_n \sim 1\ cm^2\ V^{-1}s^{-1}$), carrier transport from the semiconductor bulk to the interface itself can become limiting. Clearly a multitude of factors are important in majority carrier capture: k_{et}, acceptor concentration in the electrolyte and carrier mobility.

What about the minority carrier injection process depicted in Fig. 14? Here, contrasting with the process considered earlier, the hole injection step is usually very fast (see following). Then the current is limited by diffusion or recombination described by the Shockley equation [104]

$$i_o = \frac{e_o A D_p n_i^2}{n L_p} \tag{20a}$$

for bulk recombination, and

$$i_o = 0.5\ e_o A W \sigma v_{th} N_t n_i \tag{20b}$$

for recombination within the semiconductor space charge region. In Eqs. (20a) and (20b), D_p is the diffusion coefficient for holes, L_p is the hole diffusion length, n_i is the intrinsic carrier concentration, σ is an average capture cross-section for electrons and holes, v_{th} is the thermal velocity of charge carriers, and N_t is the areal density of recombination (trap) centers in the middle of the energy gap (Fig. 14).

The diffusion or recombination mechanism results in considerable overpotential for (cathodic) current flow in the dark (again assuming a *n*-type semiconductor for illustration). Such a rate-limiting process was found to describe the charge transfer at *n*-GaAs in 6 M HCl containing Cu^+ as the hole injecting species [55, 73].

Whatever the limiting mechanism, ultimately the current becomes limited by concentration polarization, that is, by the transport of redox species from the bulk electrolyte to the semiconductor surface. The situation in this regard is no different from that at metal electrode–electrolyte interfaces. As in the latter case, hydrodynamic voltammetry is best suited to study mass transport. AC impedance spectroscopy can be another useful tool in this regard [105].

In the former case, the data can be processed via Levich plots of current vs. $\omega^{1/2}$ (ω = angular frequency). If processes other than solution mass transport become rate-limiting, then the plot will show a curvature and the current will even become independent of the electrode rotation rate. In this case, inverse Levich (or Koutecky-Levich) plots of $1/i$ vs. $\omega^{-1/2}$ can be used for further analyses. Such analyses have been done, for example, for *n*-GaAs-acetonitrile-$Co(Cp)_2^+$ interfaces [101] and *n*- and *p*-GaAs electrodes in contact with the $Cu^{+/2+}$ redox couple in HCl electrolyte [55, 73].

The diffusion impedance at semiconductor electrodes has been considered recently [105]. This author described the applicability of AC impedance spectroscopy for the study of electron capture and hole injection processes at *n*-GaAs-H_2O/C_2H_5OH-methyl viologen, *p*-InP-aq. KOH-$Fe(CN)_6^{3}$, *n*-GaAs-H_2SO_4-Ce^{4+}, and *n*-InP-aq. KOH-$Fe(CN)_6^{3-}$ interfaces. In the case of electron capture processes, a Randles-like equivalent circuit was found to be applicable [105]. On the other hand, no Warburg component was present in the hole injection case when the reverse

reaction was negligible (Fig. 17). For a non-ideal semiconductor–electrolyte contact (see Sect. 1.3.4), a Warburg impedance appeared in the electrochemical impedance of an injection reaction as well, as exemplified by the *n*-InP-$Fe(CN)_6^{3-}$ case [105].

1.5 Light Absorption by the Semiconductor Electrode and Carrier Collection

1.5.1 Light Absorption and Carrier Generation

The optical band gap of the semiconductor (Sect. 2) is an important parameter in defining its light absorption behavior. In this quantized process, an electron-hole pair is generated in the semiconductor when a photon of energy $h\nu$ (ν = frequency and $h\nu > E_g$) is absorbed. Optical excitation thus results in a delocalized electron in the CB, leaving behind a delocalized hole in the VB; this is the band-to-band transition. Such transitions are of two types: direct and indirect. In the former, momentum is conserved and the top of VB and the bottom of CB are both located at $k = 0$ (k is the electron wave vector). The absorption coefficient (α) for such transitions is given by [106]

$$\alpha = A'(h\nu - E_g)^{1/2} \qquad (21)$$

In Eq. (21), A' is a proportionality constant. Indirect transitions involve phonon modes; in this case Eq. (21) takes the form

$$\alpha = A'(h\nu - E_g)^2 \qquad (22)$$

A given material can exhibit a direct or indirect band-to-band transition depending on its crystal structure. For example, Si single crystals have an indirect transition located at 1.1 eV (Table 1). On the other hand, amorphous Si is characterized by a direct optical transition with a larger E_g value (shorter wavelengths). Both types of transitions can also be seen in the same material, for example GaP [107].

Within the present context, the important point to note is that the absorption depths (given by $1/\alpha$) are vastly different for direct and indirect transitions. While in the former case absorption depths span the 100–1000 nm range, they can be as large as 10^4 nm for an indirect transition [9].

Optical transitions in semiconductors can also involve localized states in the band gap. These become particularly important for semiconductors in nanocrystalline form (see following). Sub–band gap transitions can be probed with photons of energy below the threshold defined by E_g.

1.5.2 Carrier Collection

The number of carriers collected (in an external circuit, for example) versus those optically generated defines the quantum yield (Φ) – a parameter of considerable interest to photochemists. The difficulty here is to quantify the amount of light actually absorbed by the semiconductor as the cell walls, the electrolyte, and other components of the assembly are all capable of either absorbing or scattering some of the incident light. Unfortunately, this problem has not been comprehensively tackled, unlike in the situation with photocatalytic reactors involving semiconductor particulate suspensions, where such analyses are available [108–111]. Pending these, an *effective* quantum yield can still be defined.

Returning to the carrier collection problem, consider Fig. 18 for an *n*-semiconductor–electrolyte interface. As can be seen, the electron-hole pairs are optically generated, both in the field-free and in the space charge regions within the semiconductor. Recombination of these

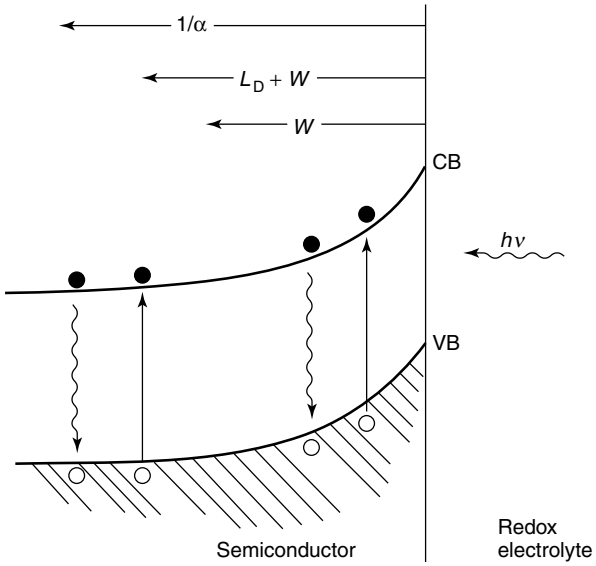

Fig. 18 Photogeneration of electron-hole pairs in the field-free region and depletion layer for a *n*-type semiconductor–electrolyte interface. The characteristic regions defined by the depletion layer (W), Debye length (L_D), and the light penetration depth ($1/\alpha$) are also compared.

carriers must be considered in the bulk, in the space charge layer, and on the semiconductor surface (the latter in contact with the redox electrolyte). We are assuming here that light is incident from the electrolyte side. Rear illumination geometry can be profitably employed and is considered later for the nanocrystalline film case.

The direction of the electric field at the interface (Fig. 6, Sect. 1.3.2) is such that the minority carriers (holes in this case) are swept to the surface and the electrons are driven to the rear ohmic contact. How fast the holes are drained away (by Faradaic reactions involving the redox electrolyte) will dictate how the Fermi levels compare with the equilibrium situation discussed earlier. The departure from equilibrium has been quantified in terms of the quasi-Fermi level concept discussed later.

The extent of collection of minority carriers from the region beyond the depletion layer is dictated by the diffusion process. A diffusion length, L, can be defined

$$L_p = \sqrt{D_p \tau_p} = \sqrt{kT \mu_p \tau_p} \quad \text{(for } n\text{-type semiconductor)} \qquad (23)$$

The subscripts in Eq. (23) remind us that we are dealing with minority carrier collection; μ_p is the hole mobility and τ_p is the hole life-time. The characteristic length L_p defines the region within which electron-hole pair generation is fully effective. Pairs generated at depths longer than the Debye length, L_D ($L_D = W + L$) will simply recombine. Thus, the effective quantum yield for a given interface will depend on the relative magnitudes of L_D and the light penetration depth, $1/\alpha$ (Fig. 18) [112, 113].

An expression for the flux of photogenerated minority carriers arriving at the surface was originally given for a solid-state junction [114] and subsequently adapted to semiconductor-liquid junctions [115]. The major weakness of these early models hinges on their underlying assumption for the boundary condition that the surface concentration of minority carriers is zero. As pointed out elsewhere [14], this is a demanding condition necessitating very high magnitudes for the interfacial charge transfer rate constant, k_{et} (see previous section). A modicum of improvement to the basic Gärtner model was found [116] by defining a flux rather than a concentration expression for the holes and a characteristic length where the bulk diffusion current transitions into a drift current. However, this treatment still assumes that every hole entering the depletion layer edge exits this region and out into the electrolyte phase.

The Gärtner equation [114] can be written in normalized form [113]

$$\Phi \equiv \frac{j_{ph}}{I_o} = 1 - \frac{\exp(-\alpha W)}{1 + \alpha L_p} \qquad (24)$$

In Eq. (24), Φ is the effective quantum yield (see previous section), given by the ratio of the photocurrent density (i_{ph}/A), j_{ph}, to the incident light flux, I_o. Recasting Eq. (24) in the form

$$-\ln(1 - \Phi) = \ln(1 + \alpha L_p) + \alpha W \qquad (25)$$

and recalling that W is proportional to $V_{SC}{}^{1/2}$ (Eq. 8), and $V_{SC} = V - V_{fb}$, a test of the rudimentary model would lie in a plot of the LHS of Eq. (25) against $(V_{fb} - V)^{1/2}$. Such plots are shown in Fig. 19 at four selected wavelengths for the p-GaP-H_2SO_4 electrolyte interface [117].

While adherence to the Gärtner model is satisfactory for large values of V_{SC} (i.e. large band bending, see Fig. 6), the model fails close to the flat band situation. Interestingly, this problem is exacerbated as the semiconductor excitation wavelength becomes shorter (Fig. 19). Thus, another weakness of the basic Gärtner model [114, 115] is the neglect of surface recombination. At the flat band situation, this model still predicts finite current flow arising from the diffusive flow of minority carriers toward and out of the interface (Fig. 20).

A variety of refinements have been made to take into account the surface recombination effect [117–132]. The earliest of these [119, 120, 123] involve some simplifying assumptions:

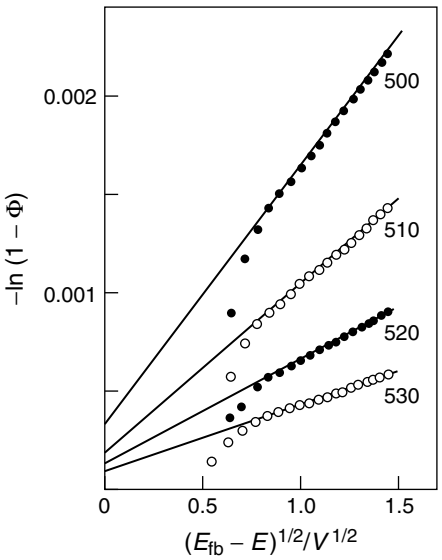

Fig. 19 Gärtner plots (see Eq. 25) for the p-GaP −0.5 M H_2SO_4 interface. The numbers on the plots refer to the excitation wavelength; E_{fb} is the flat band potential and E is the bias potential. (Note that this notation is different from that employed in the text.) (Reproduced with permission from Ref. 117.)

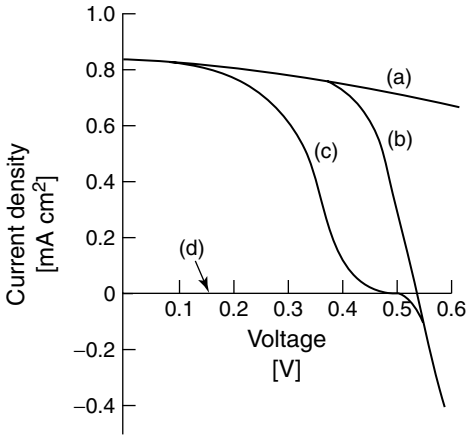

Fig. 20 Comparison of calculated current voltage profiles in the dark (curve d) and under illumination (curves a–c). Curve a is obtained from the basic Gärtner model. Curve (b) considers surface recombination and curve (c) considers both surface recombination and recombination in the space charge layer. These simulations are for a *n*-type semiconductor–electrolyte interface. (Reproduced with permission from Ref. 138.)

1. There is no recombination in the depletion layer. That is, all the holes optically generated in the bulk and within the depletion layer (Fig. 18) are swept to the surface without loss;
2. The steady state concentration of the optically generated minority carriers does not perturb the potential distribution in the dark (Fig. 6); and
3. There is a quasi-thermodynamic distribution of minority carriers within the depletion layer. This translates to a constant product term np across this region.

Surface recombination in the vast majority of these treatments invoke the Hall-Shockley-Read model [133, 134]. Defining the Gärtner limiting expression (Eq. 24) as Φ_G, we obtain [14]

$$\Phi_{ss} = \Phi_G \Big/ \left(1 + \frac{D_p \exp V_{SC}}{L_D(k_t + S_t)}\right) \quad (26)$$

In Eq. (26), we have two new parameters, k_t and S_t. These are the first-order rate constant for hole transfer (units of cm s^{-1}, see following) and the surface recombination velocity, S_t. In the combined situation of high L_D, high k_t, and very low (or zero) S_t, Eq. (26) collapses to the Gärtner limit.

At this juncture, it is worth noting that only one trap state at the surface has been assumed till now; further it is assumed that this surface state functions both as a carrier recombination site and as a charge-transfer pathway (Fig. 21). Both these assumptions are open to criticism. An alternative model invoking two distinct types of surface states – one active in recombination and the other capable of mediating charge transfer – has been considered [135]. Nonetheless, the most serious flaw in the above treatments lie in the neglect of carrier recombination in the depletion layer itself (as distinct from recombination at the surface). Reexamination of Eqs. (24) and (26) shows that the larger the Debye length, L_D, and the depletion layer width, W, the higher the quantum yield. However, recombination in the space charge layer must become significant at some value of W, thus providing a further limit to carrier collection.

Recombination within the space charge region is a nontrivial problem to treat from a computational perspective [14]. The methodology of Sah, Noyce, and Shockley [136] has been used by several authors [126, 127, 128, 131, 138–140]. Figure 20 illustrates the sensitivity of the

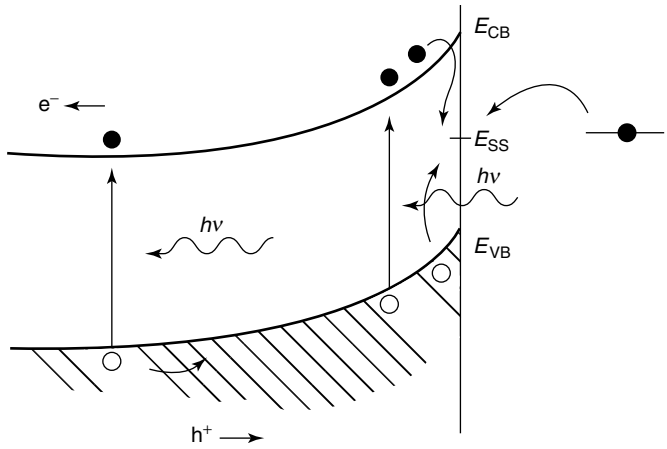

Fig. 21 Surface state mediation of both minority carrier (i.e. hole) transfer and recombination for a *n*-type semiconductor electrolyte interface.

current-potential profiles at the semiconductor–electrolyte interface to this recombination mode [137].

Other models taking the above nonidealities to varying extent have been proposed; a detailed discussion of these lies beyond the scope of this section [141–147]. However, it is worth noting here that in some instances involving high-quality semiconductor–electrolyte interfaces the rate-determining recombination step does indeed appear to lie in the bulk semiconductor [1, 148]. Silicon photoelectrodes in methanolic media containing fast, one-electron, outer-sphere redox couples were studied in these cases.

1.5.3 Photocurrent-potential Behavior

The current-voltage characteristics of an illuminated semiconductor electrode in contact with a redox electrolyte can be obtained by simply adding together the majority and minority current components. The majority carrier component is given by the diode equation (Eq. 17) while the minority carrier current (i_{ph}) is directly proportional to the photon flux (Eq. 24). Thus, the net current is given by:

$$i = i_{ph} - i_o \left[\exp\left(-\frac{e_o V}{kT} \right) - 1 \right] \quad (27)$$

The minus sign in Eq. (27) underscores the fact that the majority carrier component flows opposite (or "bucks") the minority carrier current flow. This photocurrent component is shown as curves 2 and 3 in Fig. 13.

Equation (27) shows that the diode equation is offset by the i_{ph} term; this is exactly what is seen in Fig. 13. The plateau photocurrent is proportional to the photon flux, I_o, as illustrated for two different values of the incident light intensity in Fig. 13. At the open-circuit condition of the interface, $i = 0$ (and neglecting the unity term within the square brackets relative to the exponential quantity), Eq. (27) leads to

$$V_{oc} \simeq \frac{kT}{e_o} \ln \frac{i_{ph}}{i_o} \quad (28)$$

Equation (28) underlines two important trends: First, V_{oc} increases logarithmically

with the photon flux (with a slope of ~60 mV at 298 K). Second, V_{oc} decreases with an increase of i_o (again logarithmically). This underlines the importance of ensuring that the majority carriers do not "leak" through the interface. Because of the diode nature of the interface, from a device perspective, the semiconductor surface must be designed to have fast minority carrier transfer kinetics (and thus high i_{ph}), but must be blocking to the flow of majority carriers (from the CB for a *n*-type semiconductor) into the redox electrolyte. This challenge is similar to what the solid-state device physicists face, but relative to metals (with a high density of acceptor states), *chemical* control of redox electrolytes offers a powerful route to performance optimization of liquid-based interfaces as also pointed out by previous authors [1, 6, 8, 149–154].

Referring back to Fig. 13, the current-potential curves under illumination of the semiconductor simply appear shifted "up" relative to the dark $i - V$ counterpart. This, however, is the ideal scenario. Anomalous photoeffects (APEs) are often observed that manifest as a cross-over of light and dark current-voltage curves, as illustrated in Fig. 22. Thus, the superposition principle [149–154] is not obeyed in this instance. The dashed line in Fig. 22 is produced by translating the photocurrent-voltage data by j_{SC}, the short-circuit current density. If the superposition principle is held, this dashed curve would have overlaid the dark current-voltage curve. Thus, this "excess" (forward bias) current embodies the APE, and the failure of superposition is quantified as the voltage difference (ΔV) between the dark $j - V$ data and the dashed line.

What are the ramifications of the cross-over or the APE? First, mathematical modeling of carrier transport in a junction-based solar photovoltaic system, according to

$$j = j_{SC} - j_{bk}(V) \qquad (27a)$$

is not valid in the presence of this effect. (In Eq. (27a), j_{bk} is the "bucking" current density in the forward-bias regime, see previous section.) That is, a fully linearized system of differential equations and boundary conditions cannot be used to model the interface carrier transport. Second, computation and modeling of the open-circuit voltage for such devices by

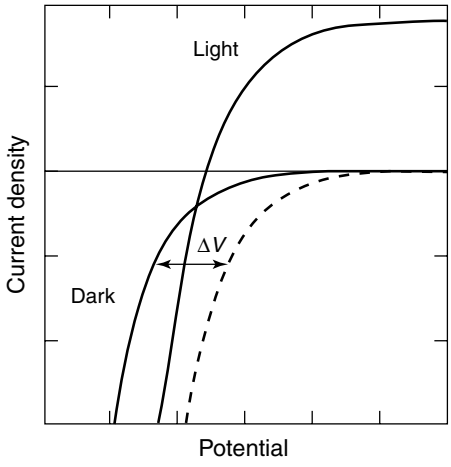

Fig. 22 Anomalous photoeffect (APE) showing cross-over of the dark and light current-voltage curves again for a *n*-type semiconductor-based interface. The dashed line is obtained as described in the text.

simply equating a constant photocurrent flux, j_{ph} against the dark (recombination) current, j_o is no longer possible (see Eq. (28) and the accompanying earlier discussion).

Third, and perhaps practically of most significance, the ΔV component represents a loss pathway in the photovoltage deliverable by the given device. Thus, the (open-circuit) photovoltage is V_{oc} instead of $V_{oc} + \Delta V$ in the ideal case in the absence of the APE. Therefore, it is important to quantify and understand the molecular and chemical origins of this effect. This has not been done so far, at least to this writer's knowledge, for semiconductor–electrolyte interfaces.

Of course, the cross-over effect is not confined to such interfaces. It is interesting that a recent textbook [155], dealing primarily with solid-state solar cell devices, makes only a fleeting reference to the underlying origin of the APE. Reference was made in this book to the cross-over of experimental dark and light $j - V$ characteristics for a Cu_2S-CdS solid-state heterojunction solar cell but its origin was not explored. A light-induced junction modification has also been reported for the (Cd, Zn)S-$CuInSe_2$ solid-state system [156, 157]. The cross-over effect appears to have been treated in even lesser depth in some classical textbooks on semiconductor devices [104, 155].

Probably the first reported instance of observation of an APE was in 1977 for a n-TiO_2-NaOH electrolyte interface [158]. The APE was observed in the saturation region of cathodic current flow and was induced by sub–band gap irradiation of the photoanode. A peak in the spectrum of the photoresponse at 800 nm (the corresponding photon energy being lower than the 3.0 eV band gap of TiO_2) was used by the authors to invoke a surface state–mediated electron transfer to O_2 (in the electrolyte) as the origin of the photoeffect. Surface states were again invoked to explain a cathodic photoeffect at n-CdS-aqueous polysulfide interfaces [159]. This photoeffect was only observed for the (0001) single-crystal face of n-CdS but not for the (0001) orientation. A subsequent study of photoelectrochemical effects at selenium films reported an anomalous *anodic* photocurrent at potentials positive of the flat band location for the p-type film [160]. This effect was assigned to a hole injection process via a tunneling mechanism. An increase of the tunneling probability under illumination was accommodated by a shrinking of the space charge layer at the interface. Photoenhancement of the forward current flow was observed again for n-CdS, in this instance in contact with a $[Fe(CN)_6]^{3-/4-}$ redox electrolyte [161]. This effect was observed only with a mechanically damaged surface, and disappeared after it had been etched with concentrated HCl.

Subsequent work [162] describes suppression of the cathodic photocurrent for n-CdS-$[Fe(CN)_6]^{3-/4-}$ interfaces mechanical polishing of the electrode. As with an earlier study [163], the spectral dependence of the photocathodic effect implicated sub–band gap states. The suppression was explained by two alternative models involving a compensated insulating layer or by Fermi-level pinning. Illumination was claimed to result in a dramatic increase of the (suppressed) cathodic current, which interestingly enough was observed only for n-CdS films but not for crystals including n-CdTe, n-CdSe, n-GaAs, n-ZnO, n-TiO_2 and n-ZnSe. On the other hand, a subsequent paper describes a photocathodic effect for n-CdSe-sulfide interfaces in which an interfacial layer of selenium was implicated [163].

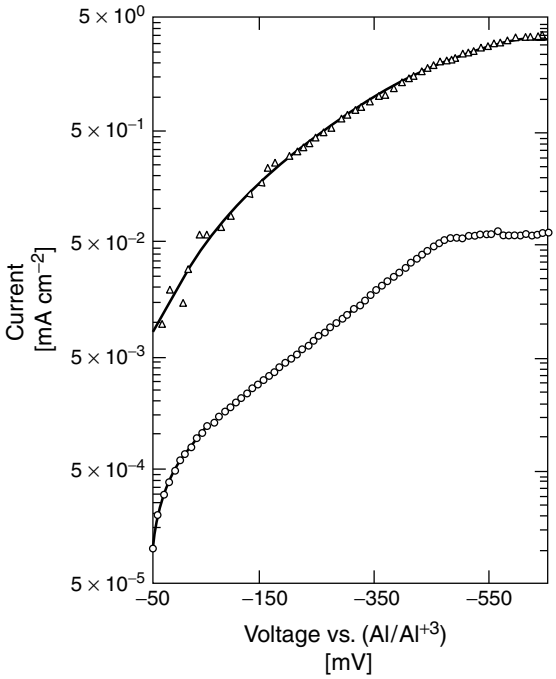

Fig. 23 Experimental data embodying APE for the *n*-GaAs-$AlCl_3$/*n*-butylpyridinium chloride molten-salt electrolyte interface. Refer to the text for details. (Reproduced with permission from Ref. 167.)

More recent studies on *n*-CdS [164, 165] and *n*-TiO_2 photoanodes [166] implicate the formation of photoconductive layers in the APEs. Thus, the foregoing review suggests the following

1. APE is a very general phenomenon that has been observed for solid-state junctions for *n*- and *p*-type semiconductors alike, and for a wide variety of semiconductor materials.
2. The reported results and trends are often contradictory. It is quite possible that the experimental conditions in these studies were quite variant, thus precluding direct comparison of the results.
3. The mechanistic reasons given for the APE are possibly many, and generalizations may not be warranted. Clearly, more research is needed on this topic.

Figure 23 contains an example of the APE for the *n*-GaAs-$AlCl_3$/*n*-butylpyridinium chloride molten salt electrolyte interface [167]. The bottom curve in Fig. 23 is the measured dark current-voltage profile. The top curve was obtained from the photocurrent-voltage data (under irradiation of the semiconductor). Clearly, if the superposition principle held, the two curves would have coincided with one another.

APEs have also been observed for nanocrystalline and chemically modified films, as discussed in a subsequent section.

Light-induced changes in the electrostatics at the semiconductor–electrolyte interface are conveniently probed by capacitance-voltage measurements in the dark and under illumination of the semiconductor electrode. If charge trapping at the interface plays a decisive role (whatever be the mechanism), the voltage

drop across the illuminated interface is altered, and consequently the semiconductor band edge positions are shifted. This, of course, is the Fermi-level pinning situation that was encountered earlier (Sect. 1.3.4). Examples of studies addressing this aspect may be found, for example on p – GaAs [124] and CdTe [168, 169]–based aqueous electrolyte interfaces.

1.5.4 Dynamics of Photoinduced Charge Transfer

So far the discussion has centered on the steady state aspects of carrier generation and collection at semiconductor–electrolyte interfaces. As with their metal electrode counterparts, a wealth of information can be gleaned from perturbation-response type of measurements. An important difference, however, lies in the vastly different timescale windows that are accessible in the two cases. The critical RC time-constant of the cell in a transient experiment is given by

$$\tau_{\text{cell}} = C(R_{\text{m}} + R_{\text{el}}) \qquad (29)$$

In Eq. (29), R_{m} is the measurement resistor (across which the current or photocurrent is measured) and R_{el} is the electrolyte resistance. The term C is the capacitance, which, in the metal case, is the Helmholtz layer capacitance, C_{H}. (Once again, the Gouy region is ignored here.) For semiconductor–electrolyte interfaces, we have seen that two layers are involved in a series circuit configuration with corresponding capacitances of C_{SC} and C_{H} (Fig. 6). Because $C_{\text{H}} \gg C_{\text{SC}}$, $C \simeq C_{\text{SC}}$. This assumption is usually justified because $C_{\text{H}} \simeq 10^{-5}$ F cm^{-2} and $C_{\text{SC}} = 10^{-8} - 10^{-0}$ F cm^{-2}. If the composite resistance $(R_{\text{m}} + R_{\text{el}})$ is 100 ohm, then τ_{cell} for metal electrodes is $\sim 10^{-3}$ s and that for the semiconductor case is $10^{-6} - 10^{-7}$ s.

What are the processes important in a dynamic interrogation of the semiconductor–electrolyte interface?

1. Carrier generation within the semiconductor,
2. diffusion of minority carriers from the field-free region to the space charge layer edge,
3. transit through this layer,
4. charge transfer across the interface, and
5. carrier recombination via surface states or via traps in the space charge layer.

Other phenomena such as thermalization also are important as discussed later in the context of hot carrier effects. The time constant (τ_{cell}) of the cell and the measurement circuitry has complicated matters further and have caused some confusion in the interpretation of transient data. If a potentiostat is not used, then this time constant is given by Eq. (29).

One can envision three types of perturbation: an infinitesimally narrow light pulse (a Dirac or δ-functional), a rectangular pulse (characteristic of chopped or interrupted irradiation), or periodic (usually sinusoidal) excitation. All three types of excitation and the corresponding responses have been treated on a common platform using the Laplace transform approach and transfer functions [170]. These perturbations refer to the temporal behavior adopted for the excitation light. However, classical AC impedance spectroscopy methods employing periodic potential excitation can be combined with steady state irradiation (the so-called PEIS experiment). In the extreme case, both the light intensity and potential can be modulated (at different frequencies) and the (nonlinear) response can be measured at sum and difference frequencies. The response parameters measured in all these cases are many but include

the photocurrent, voltage, luminescence, or microwave conductivity. Clearly, semiconductor–electrolyte interfaces present a rich, albeit demanding landscape for probing non–steady state phenomena.

The dynamics of charge transfer across semiconductor–electrolyte interfaces are considered in more detail elsewhere in this volume.

1.5.5 Hot Carrier Transfer

Short wavelength photons (of energy much greater than E_g) create "hot" carriers. If, somehow, thermalization of these carriers can be avoided, photoelectrochemical reactions that would otherwise be impossible with the "cooled" counterparts, that is, at very negative potentials for *n*-type semiconductors, would be an intriguing possibility. The key issue here is whether the rate of electron transfer across the interface can exceed the rate of hot electron cooling. The observation of hot carrier effects at semiconductor–electrolyte interfaces is a controversial matter [3, 7, 11, 171] and practical difficulties include problems with band edge movement at the interface and the like [4]. Under certain circumstances (e.g. quantum-well electrodes, oxide film-covered metallic electrodes), it has been claimed that hot carrier transfer can indeed be sustained across the semiconductor–electrolyte interface [7, 172, 173].

1.6 Multielectron Photoprocesses

This section has thus far considered redox electrolytes comprising one electron oxidizing or reducing agents. Multielectron redox processes, however, are important in a variety of scenarios. Consider the reduction of protons to H_2 (HER) – a technologically important electrochemical process that has also been extensively studied from a mechanistic perspective on metallic electrodes.

Photoelectrolytic processes such as HER can be carried out on semiconductor electrodes. One can envision a HER mechanism on a *p*-type semiconductor of the sort:

$$p - \mathrm{SC} \xrightarrow{h\nu} \mathrm{e}^-_{\mathrm{CB}} + h^+_{\mathrm{VB}} \tag{30}$$

$$\mathrm{e}^-_{\mathrm{CB}} + \mathrm{S} \longrightarrow \mathrm{S}^- \tag{30a}$$

$$\mathrm{S}^- + \mathrm{H}^+ \longrightarrow \mathrm{S} + \mathrm{H}^\bullet \tag{30b}$$

$$\mathrm{e}^-_{\mathrm{CB}} + \mathrm{H}^+ \longrightarrow \mathrm{H}^\bullet \tag{30c}$$

$$\mathrm{H}^+ + \mathrm{H}^\bullet + \mathrm{e}^-_{\mathrm{CB}} \longrightarrow \mathrm{H}_2 \tag{30d}$$

$$\mathrm{H}^+ + \mathrm{H}^\bullet + \mathrm{S}^- \longrightarrow \mathrm{H}_2 + \mathrm{S} \tag{30e}$$

$$\mathrm{h}^+_{\mathrm{VB}} + \mathrm{H}^\bullet \longrightarrow \mathrm{H}^+ \tag{30f}$$

$$\mathrm{h}^+_{\mathrm{VB}} + \mathrm{S}^- \longrightarrow \mathrm{S} \tag{30g}$$

In this above scheme, *S* denotes a surface state and both direct (Reactions 30c and 30d) and indirect (i.e. surface state–mediated) (Reactions 30b and 30e) radical and H_2-generating pathways are shown. Reactions 30f and 30g represent recombination routes involving the reaction intermediates.

Admittedly, this scheme is daunting in its complexity, and the kinetics implications are as yet unclear. Early studies on *p*-GaP, *p*-GaAs, and other Group III–V (13–15) semiconductors reported onset of cathodic photocurrents (attributable to HER) only at potentials far removed (ca. 0.6 V) from V_{fb} [174]. This was attributed to Steps 30b and 30g in the preceding scheme. More recent work [175] has shown that the HER at illuminated *p*-InP-electrolyte contacts is accompanied by a photocorrosion reaction, leading to indium formation on the semiconductor surface.

Interestingly, surface states themselves were chemically identified with $H^{\bullet}_{ads}$ (adsorbed hydrogen atom intermediates) in the aforementioned study [166]. These species have also been implicated in accumulation layer formation and anodic EL at *n*- and *p*-GaAs-electrolyte interfaces [176–178].

Another interesting characteristic of many multiequivalent redox systems is the phenomenon of photocurrent multiplication. This phenomenon may be illustrated for two systems utilizing illuminated *n*-type and *p*-type semiconductors respectively

n-type

$$n\text{-SC} \xrightarrow{h\nu} e^- + h^+ \quad (31)$$

$$HCOOH + h^+ \longrightarrow COOH^{\bullet} + H^+ \quad (31a)$$

$$COOH^{\bullet} \longrightarrow CO_2 + H^+ + e^- \quad (31b)$$

p-type

$$p\text{-SC} \xrightarrow{h\nu} h^+ + e^- \quad (31)$$

$$O_2 + H^+ + e^- \longrightarrow HO_2^{\bullet} \quad (31c)$$

$$HO_2^{\bullet} + H^+ \longrightarrow H_2O_2 + h^+ \quad (31d)$$

Thus, the key feature of photocurrent multiplication is a majority carrier injection step (Reactions 31b or 31d) from a reaction intermediate (usually a free radical) into the semiconductor CB or VB, respectively. In the preceding examples, each photon generates two carriers in the external circuit, affording a quantum yield (in the ideal case) of 2. This is the ''current-doubling'' process.

Practically, however, quantum yields somewhat lower than 2 are usually measured because Steps 31b or 31d compete with the further photooxidation or photoreduction of these intermediates, respectively. This is true especially at high photon flux values. Even multiplication factors as high as 4 are possible as in the photodissolution of *n*-Si in NH_4F media [179–182].

Photocurrent multiplication has been observed for a variety of semiconductors including Ge [180], Si [179–182], ZnO [183–189], TiO_2 [190–193], CdS [194, 195], GaP [196], InP [197], and GaAs [198–200]. These studies have included both *n*- and *p*-type semiconductors, and have spanned a range of substrates, both organic and inorganic. As in the Si case, this phenomenon can also be caused by photodissolution reactions involving the semiconductor itself. The earlier studies have mainly employed voltammetry, particularly hydrodynamic voltammetry [193]. As more recent examples [2, 9, 10] reveal, intensity-modulated photocurrent spectroscopy, (IMPS), is also a powerful technique for the study of photocurrent multiplication.

This leads us to another important category of multielectron photoprocesses involving the semiconductor itself. While photocorrosion is a nuisance from a device operation perspective, it is an important component of a device fabrication sequence in the microelectronics industry. Two types of wet etching of semiconductors can be envisioned [201]. Both occur at open-circuit but one involves the action of chemical agents that cause the simultaneous rupture and formation of bonds. Several aspects of photoetching have been reviewed [62–64, 202, 203] including reaction mechanisms, morphology of the etched surfaces, and etching kinetics in the dark and under illumination. General rules for the design of anisotropic photoetching systems have also been formulated [204]. Photoelectrochemical etching is considered in more detail elsewhere in this volume.

1.7 Nanocrystalline Semiconductor Films and Size Quantization

1.7.1 Introductory Remarks

From a materials perspective, the field of semiconductor electrochemistry and photoelectrochemistry has evolved from the use of semiconductor single crystals to polycrystalline thin films and, more recently, to nanocrystalline films. The latter have been variously termed membranes, nanoporous or nanophase films, mesoporous films, nanostructured films, and so on; they are distinguished from their polycrystalline electrode predecessors by the crystallite size (nm versus μm in the former) and by their permeability to the electrolyte phase. These films are referred to as ''nanocrystalline in the following sections. These features render three-dimensional geometry to nanocrystalline films as opposed to the ''flat'' or two-dimensional (planar) nature of single crystal or polycrystalline counterparts.

What are the virtues of these emerging photoelectrode materials? The first is related to their enormous surface area. Consider that the 3D structure is built up of close-packed spheres of radius, r. Then ignoring the void space, the specific area, A_s (area/volume) is given by $3/r$ [205]. For $r = 10\,\text{nm}$, A_s is on the order of $10^6\,\text{cm}^{-1}$, and for a $1\,\text{cm}^2$ film of $1\,\mu\text{m}$ thickness, this value corresponds to an *internal* surface area of $\sim 100\,\text{cm}^2$ (i.e. a ''surface roughness factor'' of 100). Clearly, this becomes important if we want the electrolyte redox species to be adsorbed on the electrode surface (see following). Alternatively, a large amount of sensitization dye can be adsorbed onto the support semiconductor although this dye sensitization approach is not considered in this chapter. By way of contrast, the amount of species that can be confined in a monolayer on a corresponding flat surface would be negligibly small.

As we shall see later, electron transport in nanocrystalline films is necessarily accompanied by charge-compensating cations because the holes are rapidly injected into the flooded electrolyte phase. This provides opportunities for studying ion transport processes in mesoporous media that are coupled to electron motion. Ion insertion also has practical consequences as in energy storage device applications [206].

Surface state densities on the order of $\sim 10^{12}\,\text{cm}^2$ are commonplace for semiconductor electrodes of the sort considered in previous sections of this chapter. These translate to equivalent volume densities of $\sim 10^{18}\,\text{cm}^{-3}$ for nanocrystalline films. Such high densities enhance light absorption by trapped electrons in surface states, giving rise to photochromic and electrochromic effects [198–200] (see following). Unusually high photocurrent quantum yields are also observed with sub–band gap light with these photoelectrode materials. Corresponding sub–band gap phenomena are rather weak and difficult to detect with single-crystal counterparts.

1.7.2 The Nanocrystalline Film–Electrolyte Interface and Charge Storage Behavior in the Dark

Understanding of the electrostatics across nanocrystalline semiconductor film-electrolyte junctions presents interesting challenges, particularly from a theoretical perspective. Concepts related to space charge layers, band bending, flat band potential, and the like (Sect. 3) are not applicable here because the crystallite dimensions

comprising these layers are comparable to (or even smaller than) nominal depletion layer widths.

The rather complete interpenetration of the electrode and electrolyte phases must mean that the Helmholtz double layer extends throughout the interior surface of the nanoporous network, much like a supercapacitor [9, 210] situation. Finally, unlike in the cases treated earlier, the semiconductor (especially if it is a metal oxide) is not heavily doped such that free majority carriers are not present in appreciable amounts. This is indicated, for example, by the sensitivity of the conductivity of nanocrystalline TiO_2 layers to UV light – the conductivity is strongly enhanced on UV exposure, similar to a photoconductive effect. This effect has been interpreted, in terms of trap filling with recombination times considerably slower than the trapping processes under reverse bias [211, 212]. The light sensitivity also is diagnostic of the fact that the low electronic conductivity in the dark is not due to high interparticle resistances (i.e. in the ''neck'' regions), but rather is indicative of the low electron concentrations.

The electron concentration can be increased by forward-biasing the nanocrystalline electrode–electrolyte interface potentiostatically. The interface is driven thus into the accumulation regime for the majority carriers, and if a transparent rear contact (e.g. F-doped, SnO_2 or Sn-doped indium oxide) is used, the resultant blue (or bluish-black) coloration of the film can be spectroscopically monitored [208, 209, 213]. Whether the optical response arises from CB electrons or from electrons trapped in surface states is not entirely clear. It has been claimed [214] that the absorption spectrum of the latter differs significantly from CB electrons. Electrons in surface states can be chemically identified with Ti^{3+} defect sites that can be detected, for example, by electron paramagnetic resonance spectroscopy [215, 216].

In either case, the resultant negative charge generated by electron accumulation at the internal surfaces has to be balanced by cations (from the electrolyte phase) for charge compensation. Such ion insertion reactions have been studied using techniques such as voltammetry, reflectance or absorption spectroscopy, chronoamperometry, and electrochemical quartz-crystal microgravimetry [213, 217–22]. Both aqueous and aprotic electrolytes have been deployed for these studies.

Unlike in the single-crystal cases treated earlier, placement of the semiconductor energy band positions at the interface via Mott-Schottky analyses is not straightforward for nanocrystalline films. Abrupt changes in slope and other nonidealities [215, 227, 223] have been observed, for example, in the Mott-Schottky plots for TiO_2 films and attributed to the influence of the conductive glass that is normally employed to support these films. This behavior is especially prevalent under reverse bias. The onset of majority carrier optical absorption (in the visible and near IR range) under forward-bias instead has been profitably employed to place the CB positions of TiO_2 in aqueous media [208].

Impedance spectroscopy and electrochemical dye desorption experiments have been employed [224] to study the electrical characteristics of TiO_2 nanocrystalline films in the dark. This study as well as the others cited earlier demonstrate how the conductivity changes (as a result of electron injection from the support electrode) can cause the porous or nanocrystalline layer to manifest itself electrically, such that the active region moves away (i.e. outward) from the support as the forward-bias voltage is increased. The potential

distribution has also been analyzed depending on whether the depletion layer width exceeds or is smaller than the typical dimension of the structural units in the nanocrystalline network [223].

1.7.3 Photoexcitation and Carrier Collection: Steady State Behavior

Figure 24 contains a schematic representation of the nanocrystalline semiconductor film–electrolyte interface at equilibrium (Fig. 24a) and the corresponding situation under band gap irradiation of the semiconductor (Fig. 24b) [9]. Because the diffusion length of the photogenerated carriers is usually larger than the physical dimensions of the structural units, holes and electrons can reach the impregnated electrolyte phase before they are lost via bulk recombination. This contrasts the situation with the single-crystal cases discussed earlier.

If, as is the case with TiO_2 nanocrystalline films, the holes are rapidly scavenged by the electrolyte redox (specifically Red) species, collection of the photogenerated electrons at the rear contact becomes the determinant factor in the quantum yield. Thus, the quasi-Fermi level for holes remains close to $E_{F,redox}$ and that for electrons, $E_{F,e}$ moves "up", as depicted in Fig. 24b. Illumination thus induces an electron flux, $J_n(x)$ through the nanocrystalline phase. Under steady state conditions, the photocurrent density (j_{ph}) is equal to $e_o J_n(x = d)$. The driving force for electron diffusion through the network of nanocrystallites has been calculated from first principles [225]. It has been found that the driving force is approximately kT/e_o divided by the thickness of the network. Importantly, this free-energy gradient is found to be independent of the incident photon flux.

It is important to reiterate that the charge separation in a nanocrystalline semiconductor–electrolyte interface does not depend on a built-in electric field at the junction as in the single-crystal

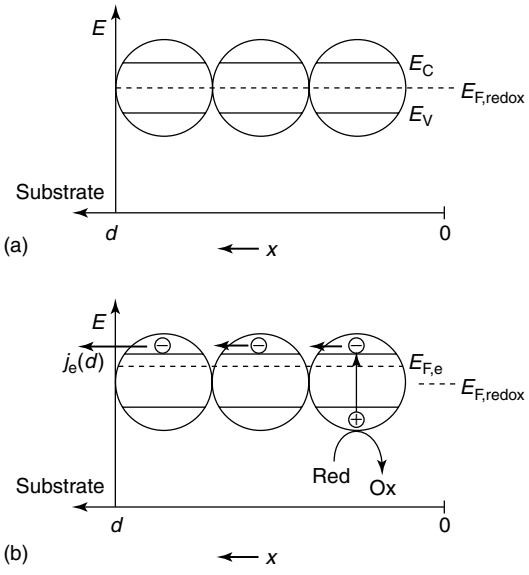

Fig. 24 Schematic representation of a nanocrystalline semiconductor–electrolyte interface in the dark (a) and under illumination from the electrolyte side (b). E_c and E_v correspond to E_{CB} and E_{VB} in our notation. (Reproduced with permission from the authors of Ref. 9.)

case. Instead, the differential kinetics for the reactions of photogenerated electrons and holes with electrolyte redox species account for the charge separation (and the generated photovoltage). The molecular factors underlying the sluggish scavenging of electrons at the nanocrystalline film-electrolyte boundary (by the redox species) are as yet unclear. Clearly, the competition between *surface* recombination of these electrons (with the photogenerated holes) and collection at the rear contact dictates the magnitude of the quantum yield that is experimentally measured for a particular junction.

Photocurrent losses have been recorded for electrolytes dosed with electron acceptors such as O_2 and iodine [226]. Nanocrystalline TiO_2 electrodes with thicknesses ranging from 2 μm to 38 μm were included in this study. In the presence of these electron-capture agents, electron collection (i.e. photocurrent) at the rear contact was seriously compromised. On the other hand, as high as 10% of the photons were converted to current for a 38 μm thick film in a N_2-purged solution [226].

The result was obtained with front-side illumination geometry. As one would intuitively expect, carrier collection is most efficient close to the rear contact. Indeed, marked differences have been observed for photoaction spectra with the two irradiation (i.e. through the electrolyte side vs. through the transparent rear contact) geometries for TiO_2, CdS, and CdSe nanocrystalline films [227, 228]. Obviously, the relative magnitudes of the excitation wavelength and the film thickness critically enter into this variant behavior.

In the vast majority of cases, the iodide/triiodide redox couple has been employed (presumably because of its success in shuttling the photooxidized dye in the sensitization experiments) although other redox electrolytes [e.g. $SCN^-/(SCN)_2{}^-$; 228] have been employed as well. For the chalcogenide films, sodium selenosulfite was employed [227]. It must be noted that, aside from losses caused by the surface recombination and back-reactions, an additional loss component from the increase in film resistance must also be recognized, especially as the film thickness is increased. The resistance loss manifests as a deterioration in the photovoltage and fill factor.

In the discussion to this point, we have not considered trapping or release of the photogenerated electrons as they undergo transit to the rear contact. However, electrons trapped in localized interfacial states induce a countercharge in the Helmholtz double-layer, as discussed in the preceding discussion. The resultant voltage drop can introduce a nonnegligible field component into the diffusional process. The time-dependence of the electron density, $n(x, t)$ is given by [9]

$$\frac{\partial n(x,t)}{\partial t} = \eta\alpha I_o e^{-\alpha x} + D_n \frac{\partial^2 n(x,t)}{\partial x^2} - \frac{n(x,t) - n_o}{\tau} \qquad (32)$$

In Eq. (32), η is the electron injection efficiency, D_n is the diffusion coefficient of electrons, and τ is the pseudo first-order lifetime of electrons determined by back-reaction with Ox.

Even if the migration component is negligible (but see following), solution of Eq. (32) presents difficulties because of the possible dependence of D_n on n and x. Similarly, τ may depend on these two variables also. Nonetheless, the steady state solution of Eq. (32) has been obtained [229] by assuming that D and τ are constant and that $\eta = 1$. Under these conditions,

the photocurrent is predicted to be independent of voltage – a rather physically implausible situation. In the forward-bias regime, η is expected to decrease and the back-reaction of the photogenerated electrons (with Ox) can no longer be neglected.

This brings us to the rear support-film interface. What sort of barrier exists at this junction? Are the electron exchange kinetics voltage-dependent at this interface? The effect of changing the work function of the substrate on the current-voltage curves (in the dark and under illumination) has been investigated for TiO_2 nanocrystalline films [230]. The onset potential for the photocurrent is found to be the same regardless of whether SnO_2, Au, or Pt is used to support the film. A Fermi level pinned *rear* interface was used to explain the results.

In general, the voltammograms for nanocrystalline electrodes are similar to what is observed for their single-crystal counterparts. An example of a photovoltammogram for CdS is contained in Fig. 25. The fact that a S-type profile is observed culminating in a photon flux-limited plateau regime is rather surprising given that (1) the film is rather insulating and (2) the electrolyte permeates into the network and possibly contacts the rear support electrode. The transition in the profiles from spiked at potentials near V_{on} (photocurrent onset) to more rectangular at positive bias potentials (not shown in Fig. 25) must mean that the voltage does exert an effect on carrier transit through the network. No satisfactory explanation appears to exist at present to resolve this apparent anomaly.

1.7.4 Photoexcitation and Carrier Collection: Dynamic Behavior

In this section, we briefly consider the response of nanocrystalline semiconductor–electrolyte interfaces to either pulsed or periodic photoexcitation. Several points are noteworthy in this respect: (1) The photocurrent rise-time in response to an illumination step is nonlinear. Further, the response is *faster* when the light intensity is higher. (2) The decay profiles exhibit features on rather slow timescales extending up to several seconds. (3) The photocurrent decay transients exhibit a peaking behavior. The time at which this peak

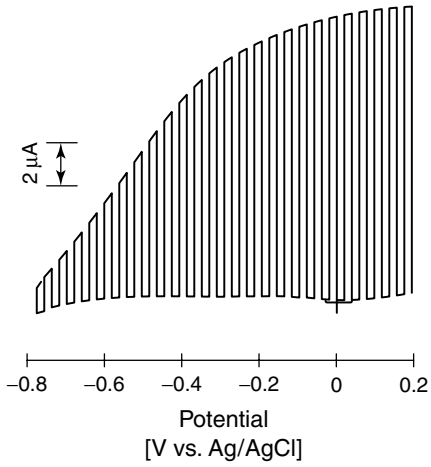

Fig. 25 Photovoltammogram under interrupted illumination of a nanocrystalline CdS-sodium sulfite electrolyte interface in the reverse-bias regime.

occurs varies with the square of the film thickness, d. (4) A similar pattern is also seen in IMPS data where the transit time, τ is seen to be proportional to d^2.

These observations have been interpreted within the framework of two distinct models, one involving trapping or detrapping of the photogenerated electrons [231, 232] and the other based on electron diffusion (or field-assisted diffusion) not attenuated by electron localization [233, 234]. The millisecond transit times also mean that the transit times are very long compared to equilibration of majority carriers in a bulk semiconductor or electron-hole pair separation within the depletion layer of a flat electrode. The slow transport is rationalized by a weak driving force and by invoking percolation effects [223].

It is interesting that the response patterns differ for different nanocrystalline electrodes [223]. For example, while trapping or detrapping effects appear to be relatively unimportant for GaP, the response for TiO_2, especially at low photon fluxes, is governed by electron trapping or detrapping kinetics. This accounts for the faster response at higher photon fluxes (see preceding section).

1.7.5 Size Quantization

When electronic particles such as electrons and holes are constrained by potential barriers to regions of space that are comparable to or smaller than their de Broglie wavelength, the corresponding allowed energy states become discrete (i.e. quantized) rather than continuous. This manifests in the absorption (or emission) spectra as discrete lines that are reminiscent of atomic (line) transitions; these sharper features often appear superimposed on a broader envelope. Another manifestation for semiconductors is that the energy band gap (E_g) increases, or equivalently, the absorption threshold exhibits a blue shift. The critical dimension for size quantization effects to appear in semiconductors depends on the effective mass (m^*) of the electronic charge carriers. For $m^* \sim 0.05$, the critical dimension is about 300 Å; it decreases approximately linearly with increasing m^* [7].

Size quantization effects and quantum dot photoelectrochemistry are discussed in more detail elsewhere in this volume.

1.8 Chemically Modified Semiconductor–Electrolyte Interfaces

1.8.1 Single Crystals

Much of the research in the early 1980s on chemically modified semiconductor–electrolyte interfaces was directed toward protecting them from photocorrosion; this body of work has been reviewed [226]. Parallel efforts also went into improving minority carrier transfer at the interface by chemisorbing metal ions such as Ru^{3+} on the semiconductor surface. Chemical agents such as sulfide ions are known to passivate the semiconductor against surface recombination [6]. A study [22a] on electron transfer dynamics at p-GaAs-acetonitrile interfaces where the semiconductor surface was sulfide-passivated exemplifies this fact. In general, the mechanistic issue of whether these chemical agents improve minority carrier charge transfer by minimizing surface recombination or by a true catalytic action has not been completely resolved [1].

Yet another tactic involves perturbing the electrostatics at the semiconductor–electrolyte interface by adsorbing

Tab. 2 A summary of approaches[a] to chemical modification of semiconductor–electrolyte interfaces

Modification agent(s)	*Semiconductor(s)*	*Modification objective*[b]	*Sample Reference(s)*
Ru^{3+}	*n*-GaAs	A	239, 240
Co^{3+}	*n*-GaAs	A	241
Os^{3+}	*n*-GaAs	A	241
Ag^{+}	*p*-InP	A	242
S^{2-}	*p*-GaAs	A	236
HS^{-}	CdS, CdSe	B	243
Thiolates	CdS, CdSe	B	244
Dithiocarbamate	CdS, CdSe	B	245, 246
Lewis acids	CdS, CdSe	B	247, 248
Lewis bases	CdS, CdSe	B	249
Cl^{-}	*n*-GaAs	B	238
Benzoic acid derivatives	n^{+}-GaAs	B	250
Noble metals	*n*-TiO_2	C	251
Noble metals	*p*-InP	C	239, 252–254
RuO_2[c]	*n*-CdS	C	255, 256
RuO_2[c]	*n*-Si	C	257
Pt[c]	*p*-Si	C	257, 258
Pt[c]	*n*-CdS	C	259
Noble metals	*n*-CdS	C	254
Noble metals[d]	*p*-InP	C	260

[a] Approaches to photoanode stabilization based on polymer films containing redox functionalities have been reviewed elsewhere, e.g. Refs. 6 and 226.
[b] A: minority carrier transfer catalysis and or surface state passivation; B: electrostatic modification; C: catalysis of multielectron photoprocesses (refer to text).
[c] In these cases, the semiconductor electrode also contained a coating, either polymeric or indium tin oxide.
[d] The chemically modified photocathode was used in conjunction with *n*-$MoSe_2$ (or *n*-WSe_2) in a two-photoelectrode cell configuration.

(or even chemically attaching) electron donors or acceptors on the semiconductor surface [237]. In favorable cases, this increases the band bending at the interface by thus introducing a fixed countercharge of opposite polarity (negative for a *n*-type semiconductor) at the junction. Chloride ion adsorption on the *n*-GaAs surface from ambient temperature $AlCl_3$/*n*-butylpyridinium chloride melts [30, 238] is a case in point; this process serves to improve the junction and the photovoltage that it delivers. Of course, such "fixed-charge" effects have long been known to the solid-state device physics and gas phase catalysis communities. Other agents that have been deployed for chemical tuning of the interfacial energetics at the semiconductor–electrolyte interface are listed in Table 2.

Native semiconductor surfaces are fairly inactive from a catalysis perspective. Thus, noble metal or metal oxide islands have been implanted on photoelectrode surfaces as electron storage centers to drive multielectron redox processes such

as HER, photooxidation of H_2O, and photooxidation of HCl, HBr, or HI. Examples of this sort of chemical modification strategy are also contained in Table 2.

The advent of self-assembled monolayer (SAM) films on electrode surfaces has rendered a high degree of molecular order and predictability to the chemical modification approach. In particular, the use of these insulating, molecular spacers enables interrogation of critical issues in electron transfer such as the influence of chemical bonding and distance between the support electrode and the redox moieties on the rate constant for electron transfer. Many such studies on gold-confined SAMs have appeared recently [261–263]. Corresponding studies on *semiconductor* surfaces (particularly Group II–V compounds such as GaAs and InP [264–266] and elemental semiconductors such as Si [267]) have also begun to appear.

Alkanethiol-based or alkylsiloxane-based SAMs have been profitably employed in all these instances to probe the distance effect in electron transfer dynamics. The thiol-based SAMs have the virtue that the spacer length can be predictably altered simply by varying the number of methylene units in the chain. The distance dependence of k_{et} is embodied in the parameter β, the decay coefficient. For a critical discussion of the subtleties involved in the extraction and interpretation of this parameter, we refer to Ref. 262. A value of 0.49 ± 0.07 has been reported for this parameter for *n*-InP-alkanethiol-ferrocyanide interfaces [266]. This value is smaller than its counterpart for corresponding films on gold surfaces, which range from ~0.6 to 1.1 per methylene unit. The reason for this difference is not entirely clear, although several hypotheses were advanced by the authors [266].

1.8.2 Nanocrystalline Semiconductor Films and Composites

Dye sensitization of nanocrystalline semiconductor films certainly represents one popular approach to chemical modification of the interface. However, this topic is covered in detail elsewhere in this volume. Other examples, from a non–dye sensitization perspective, are less common but two recent studies are noted [268, 269]. One utilizes the surface affinity of TiO_2 toward suitably derivatized viologens to construct chemically modified nanocrystalline films suitable for displays, electrochromic (smart) windows, sensors, and the like [268]. In the other study [269], the TiO_2 film surface was modified with phosphotungstic acid (PWA). This compound belongs to a family of polyoxometallates that exhibit interesting electron- and proton-transfer or storage properties and also high thermal stability [269]. Thus, these modified films would be applicable in areas such as catalysis, sensors, electronics, and even medicine.

These TiO_2-PWA films represent a logical bridge connecting single-phase semiconductor films and multicomponent composite systems. Of course, highly evolved multicomponent assemblies occur in nature and there is no better example than the plant photosynthetic system. The plant photosynthetic architecture contains synergistic components (e.g. light-harvesting antennae, membranes) each with a well-defined and complementary function, to convert the incident photon energy, to move electrons vectorially, and to store the reaction products. The design and implementation of artificial analogs have proved to be a daunting task, both from a synthetic and characterization perspective. While this topic is covered

elsewhere in this series of volumes, we briefly discuss in what follows, some simple multicomponent assemblies based on semiconductors.

Early examples in the 1980s were aimed at the design of composite systems for photoelectrolytic generation of H_2. Thus, Nafion and SiO_2 were used as supports for coprecipitated ZnS and CdS for photoassisted HER from aqueous sulfide media [270]. Subsequent work has addressed the mechanistic role of the support in the photoassisted HER [271]. Vectorial electron transfer was demonstrated in bipolar TiO_2/Pt or CdSe/CoS photoelectrode panels arranged in series arrays for the photodecomposition of water to H_2 and O_2 [272, 273].

More recently, matrix-semiconductor composites, that is, films comprising of semiconductor particles that are dispersed in a nonphotoactive continuous matrix have been developed. Examples of matrix candidates are metals and polymers [274–279]. Occlusion electrosynthesis is a versatile method for preparing such composite films as exemplified by the Ni/TiO_2 and Ni/CdS family [280–282].

Matrix-semiconductor composite films have two virtues from a photoelectrochemical perspective. First, their components can be separately chosen and optimized for a specific function. Thus, the matrix component can be chosen to have good adsorption tendency toward a targeted substrate. The semiconductor component then functions in the role of photogenerating charge carriers either for reducing or oxidizing this sequestered substrate. This photocatalytic strategy has been recently demonstrated both for organic substrates (methanol and formate ion) [283, 284] and an inorganic substrate (sulfite) [285]. The net result in either case is an enhanced photocatalytic performance of the composite because of the high *local* concentration of the substrate resulting from the matrix adsorption process. In principle, high surface area supports of the sort that are normally used in the gas-phase catalysis community can also be used in conjunction with TiO_2 [286, 287]. These would include materials such as Al_2O_3, SiO_2, or diatomaceous earth. The resultant composite films, however, cannot be used as electrodes because of their poor electronic conductivity.

The second important feature of a metal-semiconductor composite approach is that the metal can function as a template for chemical or electrochemical derivatization to afford a film comprising molecular redox-semiconductor (or even semiconductor-semiconductor) contacts. Figure 26 generically illustrates the occlusion electrosynthesis approach for preparing M/TiO_2 composite films and a subsequent derivatization with ferri/ferrocyanide to afford the corresponding metal hexacyanoferrate (MHCF)/TiO_2 counterparts [288]. These chemically modified films exhibit interesting ''bipolar'' photoelectrochemical behavior [289] and photoelectrochromic properties [290].

1.9 Types of Photoelectrochemical Devices

As Fig. 27 illustrates, there are basically three types of photoelectrochemical devices for solar energy conversion. The first type is regenerative in nature and the species that are photooxidized at the *n*-type semiconductor electrode are simply re-reduced at the counterelectrode (Fig. 27a). Instead of an electrocatalytic electrode [291, 292] where the counterelectrode reaction occurs in the dark (this is the situation schematized

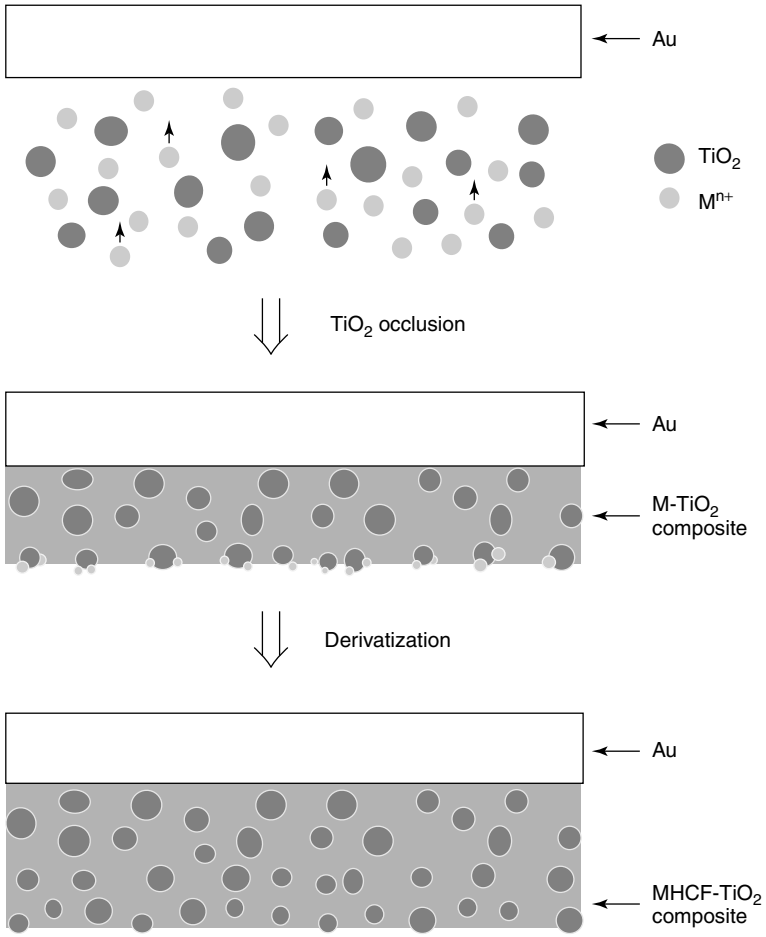

Fig. 26 Schematic illustration of the occlusion electrosynthesis approach for the preparation of M/TiO_2 (M = metal) composite films and subsequent chemical derivatization to yield the $MHCF/TiO_2$ counterparts. Refer to the text for further details.

in Fig. 27a), a *p*-type semiconductor photo-cathode may also be deployed in a tandem regenerative cell. In all these cases, the cells operate in the photovoltaic mode where the input photon energy is converted into electricity.

Interesting enough, it is the second type of device, namely a photoelectrolytic cell (Fig. 27b), that first caught the attention of a scientific and technological community in the 1970s that was searching for alternative energy sources to fossil-derived fuels. Thus in a landmark paper, Fujishima and Honda [293] demonstrated that sunlight could be used to drive the photoelectrolysis of water using an *n*-TiO_2 photoanode and a Pt counterelectrode. Unfortunately, the requirements for efficiently splitting water are rather stringent, as discussed elsewhere in this volume.

In the third type of energy conversion device, the initial photoexcitation does not

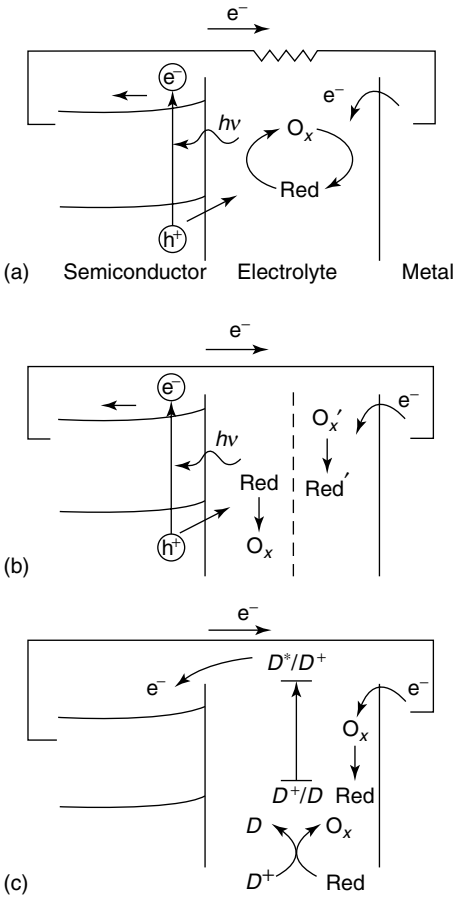

Fig. 27 Types of photoelectrochemical devices for solar energy conversion. (a), (b), and (c) depict regenerative, photoelectrolytic, and dye-sensitized configurations, respectively. As in the remainder of this chapter, an *n*-type semiconductor is assumed in these cases for specificity.

occur in the semiconductor (unlike in the device counterparts in Figs. 27a and b) but occurs instead in a visible light-absorbing dye (Fig. 27c). Subsequent injection of an electron from the photoexcited dye into the semiconductor CB results in the flow of a current in the external circuit. Sustained conversion of light energy is facilitated by regeneration of the reduced form of the dye via a reversible redox couple (e.g. iodide/triiodide) [294]. Therefore, this device, as its counterpart in Fig. 27(a), also operates in a photovoltaic mode, or perhaps more appropriately, in a *photogalvanic* mode.

Other variants of the three types of device operation may be envisioned for semiconductor-liquid junctions. Thus, in the photoelectrolytic mode, the cell reaction clearly is driven (by light) in the contrathermodynamic direction, that is, $\Delta G > 0$. However, there are many instances, involving, for example, the photooxidation of organic compounds in which light merely serves to accelerate the reaction rate. Thus these cells operate in the photocatalytic mode. In fact, aqueous suspensions comprising irradiated semiconductor particles may be considered to be an assemblage of short-circuited microelectrochemical cells operating in the photocatalytic mode.

Finally, a storage electrode may be incorporated even in a regenerative photoelectrochemical cell of the sort schematized in Fig. 27(a). Thus, when the sun is shining, this storage electrode is "charged"; in the dark, energy may be tapped (as from a battery) from this storage electrode [295–298].

Further details of these device types as well as *nonenergy*-related applications of photoelectrochemical cells (such as in environmental remediation) may be found in the chapters that follow in this volume.

1.10 Conclusion

In this introductory chapter, we have discussed the electrostatics of the semiconductor–liquid interface considering both single crystals as well as their nanocrystalline counterparts. The charge

transfer dynamics across both these types of interfaces have been described in the dark and under photoexcitation of the semiconductor. Finally, the various types of photoelectrochemical devices for solar energy conversion are introduced. Subsequent chapters in this volume provide further elaboration of some of these topics considered herein.

Acknowledgments

Research in the author's laboratory on semiconductor electrochemistry and photoelectrochemistry since 1995 is funded, in part, by the Office of Basic Energy Sciences, the US Department of Energy. A number of talented and dedicated coworkers and colleagues have been involved in collaborative research with the author over the past twenty years; their names appear in the publications cited from this laboratory. I also thank the University of Texas at Arlington for providing the facilities and infrastructure. I am grateful to Prof. S. Licht for comments on an earlier version of the manuscript. Last but not least, I thank Ms. Gloria Madden and Ms. Rita Anderson for assistance in the preparation of this chapter.

References

1. N. S. Lewis, *Acc. Chem. Res.* **1990**, *23*, 176.
2. L. M. Peter, *Chem. Rev.* **1990**, *90*, 753.
3. N. S. Lewis, *Annu. Rev. Phys. Chem.* **1991**, *42*, 543.
4. C. A. Koval, J. N. Howard, *Chem. Rev.* **1992**, *92*, 411.
5. A. Kumar, W. C. Á. Wilisch, N. S. Lewis, *Crit. Rev. Solid State Mater. Sci.* **1993**, *18*, 327.
6. M. X. Tan, P. E. Laibinis, S. T. Nguyen et al., *Prog. Inorg. Chem.* **1994**, *41*, 21.
7. A. J. Nozik, R. Memming, *J. Phys. Chem.* **1996**, *100*, 13061.
8. N. S. Lewis, *J. Phys. Chem.* **1998**, *102*, 4843.
9. L. M. Peter, D. Vanmaekelbergh, *Adv. Electrochem. Sci. Eng.* **1999**, *6*, 77.
10. L. M. Peter in *Comprehensive Chemical Kinetics*, (Eds.: R. G. Compton, G. Hancock), Elsevier, Amsterdam, 1999, pp. 223–280.
11. R. J. D. Miller, G. McLendon, A. J. Nozik et al., in *Surface Electron-transfer Processes*, VCH Publishers, New York, 1995.
12. K. Rajeshwar, L. M. Peter, A. Fujishima et al., Eds., in *Photoelectrochemistry Proc.*, The Electrochemical Society, Pennington, NJ, 1997, Vol. 20.
13. N. Sato in *Electrochemistry at Metal and Semiconductor Electrodes*, Elsevier, Amsterdam, 1998.
14. A. Hamnett in *Comprehensive Chemical Kinetics* (Eds.: R. G. Compton), Elsevier, Amsterdam, 1987, p. 61, Vol. 27.
15. J. S. Newman in *Electrochemical Systems*, 2nd edition, Prentice-Hall, Englewood Cliffs, NJ, 1991, p. 496.
16. R. A. Smith in *Semiconductors*, Cambridge University Press, Cambridge, 1964.
17. F. A. Kröger, H. J. Vink in *Solid State Physics* (Eds.: F. Seitz, D. Turnbull), Academic Press, New York, 1956, Vol. 3.
18. F. A. Kröger in *The Chemistry of Imperfect Crystals*, North Holland, Amsterdam, 1964.
19. N. B. Hannay, Ed., in *Semiconductors*, Reinhold, New York, 1959.
20. A. R. West in *Solid State Chemistry and Its Applications*, John Wiley, New York, 1984.
21. P. A. Cox in *The Electronic Structure and Chemistry of Solids*, Oxford University Press, Oxford, England, 1987.
22. R. Hoffmann in *Solids and Surfaces*, VCH, New York and Weinheim, 1988.
23. K. Uosaki, H. Kita in *Modern Aspects of Electrochemistry* (Eds.: R. E. White, J. O'M. Bockris, B. E. Conway), Plenum, New York, 1986, pp. 1–60, Vol. 18.
24. S. Trasatti in *The Absolute Electrode Potential: An Explanatory Note*, IUPAC Commission I.3 (Electrochemistry), 1984.
25. H. Reiss, *J. Electrochem. Soc.* **1978**, *125*, 937.
26. Yu. V. Pleskov, Yu. Ya. Gurevich in *Semiconductor Photoelectrochemistry*, Consultants Bureau, New York, 1986.
27. H. Gerischer, *Adv. Electrochem. Eng.* **1961**, *1*, 139.
28. H. Gerischer in *Physical Chemistry: An Advanced Treatise* (Eds.: H. Eyring, D. Henderson, W. Jost), Academic Press, New York, 1970, Vol. 9A.

29. S. R. Morrison in *The Chemical Physics of Surfaces*, Plenum, New York and London, 1977.
30. P. Singh, R. Singh, R. Gale et al., *J. Appl. Phys.* **1980**, *51*, 6286.
31. K. Rajeshwar in *Molten Salt Techniques* (Eds.: R. J. Gale, D. G. Lovering), Plenum, New York and London, 1984, pp. 221–252, Vol. 2.
32. R. Thapar, K. Rajeshwar, *Electrochim. Acta* **1983**, *28*, 198.
33. C. M. Gronet, N. S. Lewis, G. W. Cogan et al., *J. Electrochem. Soc.* **1984**, *131*, 2873.
34. E. H. Rhoderick in *Metal-Semiconductor Contacts*, Clarendon Press, Oxford, 1980.
35. S. Kar, K. Rajeshwar, P. Singh et al., *Sol. Energy* **1979**, *23*, 129.
36. G. Horowitz, P. Allongue, H. Cachet, *J. Electrochem. Soc.* **1984**, *131*, 2563.
37. A. J. Bard, A. B. Bocarsly, F. R. F. Fan et al., *J. Am. Chem. Soc.* **1980**, *102*, 3671.
38. A. Many, Y. Goldstein, N. B. Grover in *Semiconductor Surfaces*, North Holland, Amsterdam, 1965.
39. G. A. Somorjai in *Introduction to Surface Chemistry and Catalysis*, John Wiley, New York, 1994.
40. A. W. Adamson, A. P. Gast in *Physical Chemistry of Surfaces*, John Wiley, New York, 1997.
41. R. L. Van Meirhaeghe, F. Cardon, W. P. Gomes, *J. Electroanal. Chem.* **1985**, *188*, 287.
42. J. Bardeen, *Phys. Rev.* **1947**, *71*, 717.
43. A. M. Cowley, S. M. Sze, *J. Appl. Phys.* **1965**, *36*, 3212.
44. S. Kurtin, T. C. McGill, C. A. Mead, *Phys. Rev. Lett.* **1969**, *22*, 1433.
45. T. C. McGill, *J. Vac. Sci. Technol.* **1974**, *11*, 935.
46. L. J. Brillson, *Phys. Rev. Lett.* **1978**, *40*, 260.
47. L. J. Brillson, *J. Vac. Sci. Technol.* **1979**, *16*, 1137.
48. W. E. Spicer, P. W. Chye, P. R. Skeath et al., *J. Vac. Sci. Technol.* **1979**, *16*, 1422.
49. G. Nogami, *J. Electrochem. Soc.* **1982**, *129*, 2219.
50. K. Uosaki, H. Kita, *J. Electrochem. Soc.* **1983**, *130*, 895.
51. R. de Gruyse, W. P. Gomes, F. Cardon et al., *J. Electrochem. Soc.* **1975**, *125*, 711.
52. J. C. Tranchart, L. Hollan, R. Memming, *J. Electrochem. Soc.* **1978**, *125*, 1185.
53. S. R. Morrison, *Surf. Sci.* **1969**, *15*, 363.
54. R. A. L. Vanden Berghe, F. Cardon, W. P. Gomes, *Surf. Sci.* **1973**, *39*, 368.
55. D. Meissner, R. Memming, *Electrochim. Acta* **1992**, *37*, 799.
56. H. Gerischer, *Ber. Bunsen-Ges. Phys. Chem.* **1965**, *69*, 578.
57. R. Memming, G. Schwandt, *Electrochim. Acta* **1968**, *13*, 1299.
58. M. J. Madou, F. Cardon, W. P. Gomes, *Ber. Bunsen-Ges. Phys. Chem.* **1977**, *81*, 1186.
59. H. H. Goossens, W. P. Gomes, *J. Electrochem. Soc.* **1991**, *138*, 1696.
60. D. Vanmaekelbergh, L. S. Yun, W. P. Gomes et al., *J. Electroanal. Chem.* **1987**, *221*, 187.
61. J. J. Kelly, J. E. A. M. van den Meerakker, P. H. L. Notten et al., *Philips Tech. Rev.* **1988**, *44*, 61.
62. P. H. L. Notten, J. E. A. M. van den Meerakker, J. J. Kelly in *Etching of III-V Semiconductors: An Electrochemical Approach*, Elsevier, Oxford, 1991.
63. H. H. Goossens, W. P. Gomes, *Electrochim. Acta* **1992**, *37*, 811.
64. W. P. Gomes, H. H. Goossens in *Adv. Electrochem. Sci. Eng.* (Eds.: H. Gerischer, C. W. Tobias), VCH, Weinheim, 1994, Vol. 3.
65. D. Meissner, C. Sinn, R. Memming et al., in *Homogeneous Photocatalysis* (Eds.: E. Pelizetti, N. Serpone, D. Reidel), Dordrecht, 1986.
66. J. E. A. M. van den Meerakker, *J. Electroanal. Chem.* **1988**, *243*, 161.
67. B. Pettinger, H-R. Schöppel, H. Gerischer, *Ber. Bunsen-Ges. Phys. Chem.* **1976**, *80*, 849.
68. K. Uosaki, *Trends Anal. Chem.* **1990**, *9*, 98.
69. K. Uosaki, H. Kita, *Ber. Bunsen-Ges. Phys. Chem.* **1984**, *91*, 447.
70. A. Manivannan, A. Fujishima, *J. Lumin.* **1988**, *42*, 43.
71. G. Oskam, E. A. Meulenkamp, *J. Electroanal. Chem.* **1992**, *326*, 213.
72. R. Reincke, R. Memming, *J. Phys. Chem.* **1992**, *96*, 1310.
73. R. Reineke, R. Memming, *J. Phys. Chem.* **1992**, *96*, 1317.
74. J. Vandermolen, W. P. Gomes, F. Cardon, *J. Electrochem. Soc.* **1980**, *127*, 324.
75. P. Salvador, C. Gutierrez, *J. Electrochem. Soc.* **1984**, *131*, 326.
76. V. A. Tyagai, G. Ya. Kolbasov, *Surf. Sci.* **1971**, *28*, 423.

77. W. P. Gomes, F. Cardon, *Ber. Bunsen-Ges. Phys. Chem.* **1970**,*74*, 431.
78. Z. Hens, *J. Phys. Chem. B* **1999**, *103*, 122.
79. Z. Hens, W. P. Gomes, *J. Phys. Chem. B* **1999**, *103*, 130.
80. F. Cardon, *Physica* **1972**, *57*, 390.
81. G. Horowitz, *J. Electroanal. Chem.* **1983**, *159*, 421.
82. D. Vanmaekelbergh, *Electrochim. Acta* **1997**, *42*, 1135.
83. Z. Hens, W. P. Gomes, *Electrochim. Acta* **1998**, *43*, 2577.
84. W. P. Gomes, D. Vanmaekelbergh, *Electrochim. Acta* **1996**, *41*, 967.
85. P. A. Allongue, H. Cachet, *J. Electrochem. Soc.* **1985**, *132*, 45.
86. J. E. A. M. Van der Meerakker, J. J. Kelly, P. H. L. Notten, *J. Electrochem. Soc.* **1985**, *132*, 638.
87. K. Schröder, R. Memming, *Ber. Bunsen-Ges. Phys. Chem.* **1985**, *89*, 385.
88. D. Vanmaekelbergh, W. P. Gomes, F. Cardon, *Ber. Bunsen-Ges. Phys. Chem.* **1986**, *90*, 431.
89. D. Vanmaekelbergh, W. P. Gomes, F. Cardon, *Ber. Bunsen-Ges. Phys. Chem.* **1985**, *89*, 994.
90. D. Vanmaekelbergh, W. P. Gomes, F. Cardon, *J. Electrochem. Soc.* **1987**, *134*, 891.
91. D. Vanmaekelbergh, R. P. ter Heide, W. Kruijt, *Ber. Bunsen-Ges. Phys. Chem.* **1989**, *93*, 1103.
92. D. Vanmaekelbergh, F. Cardon, *J. Phys. D: Appl. Phys.* **1986**, *19*, 643.
93. D. Vanmaekelbergh, F. Cardon, *Semicond. Sci. Technol.* **1988**, *3*, 124.
94. J. J. Kelly, P. H. L. Notten, *Electrochim. Acta* **1984**, *29*, 589.
95. J. E. A. M. van den Meerakker, *Electrochim. Acta* **1985**, *30*, 435.
96. A. M. Fajardo, N. S. Lewis, *Science* **1996**, *274*, 969.
97. A. M. Fajardo, N. S. Lewis, *J. Phys. Chem. B* **1997**, *101*, 11136.
98. K. E. Pomykal, N. S. Lewis, *J. Phys. Chem. B* **1997**, *101*, 2476.
99. A. Meier, S. S. Kocha, M. C. Hanna et al., *J. Phys. Chem. B* **1997**, *101*, 7038.
100. I. Uhlendorf, R. Reincke-Koch, R. Memming, *J. Phys. Chem.* **1996**, *100*, 4930.
101. A. Meier, D. C. Selmarten, K. Siemoneit et al., *J. Phys. Chem. B* **1999**, *103*, 2122.
102. Y. Rosenwaks, B. R. Thacker, R. K. Ahrenkiel et al., *J. Phys. Chem.* **1992**, *96*, 10096.
103. H. Gerischer, *J. Phys. Chem.* **1991**, *95*, 1356.
104. S. M. Sze in *Physics of Semiconductor Devices*, John Wiley, New York, 1981.
105. Z. Hens, W. P. Gomes, *J. Phys. Chem. B* **1997**, *101*, 5814.
106. J. L. Pankove in *Optical Processes in Semiconductors*, Prentice Hall, Englewood Cliffs, NJ, 1971.
107. D. Vanmaekelbergh, B. H. Erne, C. W. Cheung et al., *Electrochim. Acta* **1995**, *40*, 686.
108. I. Rosenberg, J. R. Brock, A. Heller, *J. Mol. Catal.* **1992**, *96*, 3423.
109. J. Valladares, J. R. Bolton in *Photocatalytic Purification and Treatment of Water and Air* (Eds.: D. F Ollis, H. Al-Ekabi), Elsevier, Amsterdam, 1993, p. 111.
110. M. I. Cabrera, O. M. Alfano, A. E. Cassano, *J. Phys. Chem.* **1996**, *100*, 20043.
111. C. A. Martin, M. A. Baltanas, A. E. Casano, *Environ. Sci. Technol.* **1996**, *30*, 2355.
112. K. Rajeshwar, *Spectroscopy* **1993**, *8*, 16.
113. L. M. Peter in *Comprehensive Chemical Kinetics* (Eds.: R. G. Compton), Elsevier, Amsterdam, 1989, pp. 353–383, Vol. 29.
114. W. W. Gärtner, *Phys. Rev.* **1959**, *116*, 84.
115. M. A. Butler, *J. Appl. Phys.* **1977**, *48*, 1914.
116. V. A. Tyagai, *Russ. J. Phys. Chem.* **1965**, *38*, 1335.
117. J. Li, L. M. Peter, *J. Electroanal. Chem.* **1984**, *165*, 41.
118. L. M. Peter, J. Li, R. Peat, *J. Electroanal. Chem.* **1984**, *165*, 29–41.
119. R. H. Wilson, *CRC Crit. Rev. Solid State Mater. Sci.* **1980**, *10*, 1.
120. R. H. Wilson, *J. Appl. Phys.* **1977**, *48*, 4297.
121. K. Rajeshwar, *J. Electrochem. Soc.* **1980**, *129*, 1003.
122. J. F. McCann, D. Haneman, *J. Electrochem. Soc.* **1982**, *129*, 1134.
123. R. Memming, *Surf. Sci.* **1964**, *1*, 88.
124. J. J. Kelly, R. Memming, *J. Electrochem. Soc.* **1982**, *129*, 730.
125. S. U. M. Khan, J. O'M. Bockris, *J. Phys. Chem.* **1984**, *88*, 2504.
126. F. E. Guibaly, K. Colbow, B. L. Funt, *J. Appl. Phys.* **1981**, *52*, 3480.
127. F. E. Guibaly, K. Colbow, *J. Appl. Phys.* **1982**, *53*, 1737.
128. F. E. Guibaly, K. Colbow, *J. Appl. Phys.* **1983**, *54*, 6488.
129. J-N. Chazalviel, *J. Electrochem. Soc.* **1982**, *129*, 963.

130. M. Nishida, *J. Appl. Phys.* **1980**, *51*, 1669.
131. F. E. Guibaly, K. Colbow, *Can. J. Phys.* **1981**, *59*, 1682.
132. D. L. Ullman, *J. Electrochem. Soc.* **1981**, *128*, 1269.
133. S. Ramakrishna, S. K. Rangarajan, *J. Electroanal. Chem.* **1991**, *308*, 49.
134. W. Shockley, W. T. Read, *Phys. Rev.* **1952**, *87*, 835.
135. R. N. Hall, *Phys. Rev.* **1982**, *87*, 387.
136. S. J. Fonash in *Solar Cell Device Physics*, Academic Press, San Diego, 1981, Chapter 6, pp. 262–326.
137. C. T. Sah, R. N. Noyce, W. Shockley, *Proc. IRE* **1957**, *45*, 1228.
138. J. Reichman, *Appl. Phys. Lett.* **1980**, *36*, 574.
139. W. I. Albery, P. N. Bartlett, A. Hamnett et al., *J. Electrochem. Soc.* **1981**, *128*, 1492.
140. W. J. Albery, P. N. Bartlett, *J. Electrochem. Soc.* **1983**, *130*, 1699.
141. H. Reiss, *J. Electrochem. Soc.* **1978**, *125*, 937.
142. J. Thomchick, A. M. Buoncristiani, *J. Appl. Phys.* **1980**, *51*, 6265.
143. W. Lorenz, M. Handschuh, *J. Electroanal. Chem.* **1980**, *111*, 181.
144. W. Lorenz, C. Aegerter, M. Handschuh, *J. Electroanal. Chem.* **1987**, *221*, 33.
145. M. Handschuh, W. Lorenz, *J. Electroanal. Chem.* **1988**, *251*, 1.
146. P. Lemasson, A. Etcheberry, J. Gautron, *Electrochim. Acta* **1982**, *27*, 607.
147. S. Ramakrishna, S. K. Rangarajan, *J. Electroanal. Chem.* **1994**, *369*, 289.
148. M. L. Rosenbluth, C. M. Lieber, N. S. Lewis, *Appl. Phys. Lett.* **1984**, *45*, 423.
149. S. Licht, *Nature* **1987**, *330*, 148.
150. S. Licht, D. Peramunage, *Nature* **1990**, *345*, 330.
151. S. Licht, N. Myung, *J. Electrochem. Soc.* **1995**, *142*, 840.
152. S. Licht, N. Myung, *J. Electrochem. Soc.* **1995**, *142*, 845.
153. S. Licht, F. Forouzan, *J. Electrochem. Soc.* **1995**, *192*, 1539.
154. S. Licht, D. Peramunage, *J. Phys. Chem. B* **1996**, *100*, 9082.
155. H. J. Hovel in *Semiconductors and Semimetals, Solar Cells*, Academic Press, New York, 1975, Vol. 11.
156. R. R. Potter, J. R. Sites, *IEEE Trans. Electron Devices* **1984**, *ED-31*, 571.
157. R. R. Potter, J. R. Sites, *Appl. Phys. Lett.* **1983**, *43*, 843.
158. H. Morisaki, M. Hariya, K. Yazawa, *Appl. Phys. Lett.* **1977**, *30*, 7.
159. H. Minoura, M. Tsuiki, *Chem. Lett.* **1978**, 205.
160. W. Gissler, *J. Electrochem. Soc.* **1980**, *127*, 1713.
161. B. Vainas, G. Hodes, J. DuBow, *J. Electroanal. Chem.* **1981**, *130*, 391.
162. N. Müller, G. Hodes, B. Vainas, *J. Electroanal. Chem.* **1984**, *172*, 155.
163. R. Tenne, W. Giriat, *J. Electroanal. Chem.* **1985**, *186*, 127.
164. D. P. Amalnerkar, S. Radhakrishnan, H. Minoura et al., *Sol. Energy Mater.* **1988**, *18*, 37.
165. D. P. Amalnerkar, S. Radhakrishnan, H. Minoura et al., *J. Electroanal. Chem.* **1989**, *260*, 433.
166. S.-E. Lindquist, H. Vidarsson, *J. Mol. Catal.* **1986**, *38*, 131.
167. P. Singh, R. Singh, K. Rajeshwar et al., *J. Electrochem. Soc.* **1981**, *128*, 1145.
168. D. Lincot, J. Vedel, *J. Electroanal. Chem.* **1987**, *220*, 179.
169. D. Lincot, J. Vedel, *J. Phys. Chem.* **1988**, *92*, 4103.
170. L. M. Peter in *Photocatalysis and the Environment* (Ed.: M. Schiavello), Kluwer Academic Publishers, Dordrecht, 1988, p. 243, Vol. 237.
171. B. Ba, H. Cachet, B. Fotouhi et al., *Electrochim. Acta* **1992**, *37*, 309.
172. Y-E. Sung, F. Galliard, A. J. Bard, *J. Phys. Chem. B* **1998**, *102*, 9797.
173. Y-E. Sung, A. J. Bard, *J. Phys. Chem. B* **1998**, *102*, 9806.
174. M. P. Dare-Edwards, A. Hamnett, J. B. Goodenough, *J. Electroanal. Chem.* **1981**, *119*, 109.
175. J. Schefold, *J. Phys. Chem.* **1992**, *96*, 8692.
176. K. Uosaki, H. Kita, *J. Am. Chem. Soc.* **1986**, *108*, 4294.
177. S. Kaneko, K. Uosaki, H. Kita, *J. Phys. Chem.* **1986**, *90*, 6654.
178. K. Uosaki, Y. Shigematsu, S. Kaneko et al., *J. Phys. Chem.* **1989**, *93*, 6521.
179. M. Matsumura, S. R. Morrison, *J. Electroanal. Chem.* **1983**, *144*, 113.
180. M. Matsumura, S. R. Morrison, *J. Electroanal. Chem.* **1983**, *147*, 157.
181. H. J. Lewerenz, J. Stumper, L. M. Peter, *Phys. Rev. Lett.* **1988**, *61*, 1989.
182. L. M. Peter, A. N. Borazio, H. J. Lewerenz et al., *J. Electroanal. Chem.* **1990**, *290*, 229.

183. S. R. Morrison, T. Freund, *J. Chem. Phys.* **1967**, *47*, 1543.
184. W. P. Gomes, T. Freund, S. R. Morrison, *Surf. Sci.* **1968**, *13*, 201.
185. W. P. Gomes, T. Freund, S. R. Morrison, *J. Electrochem. Soc.* **1968**, *115*, 818.
186. K. Micka, H. Gerischer, *J. Electroanal. Chem.* **1972**, *38*, 397.
187. J.-S. Lee, T. Kato, A. Fujishima et al., *Bull. Chem. Soc. Jpn.* **1984**, *57*, 1179.
188. G. H. Schoenmakers, D. Vanmaekelbergh, J. J. Kelly, *J. Phys. Chem.* **1996**, *100*, 3215.
189. G. H. Schoenmakers, D. Vanmaekelbergh, J. J. Kelly, *J. Chem. Soc., Faraday Trans.* **1997**, *93*, 1127.
190. M. Miyake, H. Yoneyama, H. Tamura, *Chem. Lett.* **1976**, 635.
191. N. Hykaway, W. M. Sears, H. Morisaki et al., *J. Phys. Chem.* **1986**, *90*, 6663.
192. D. J. Fermin, E. A. Ponomarev, L. M. Peter, in *Photoelectrochemistry, Proc.*, (Eds.: K. Rajeshwar, L. M. Peter, A. Fujishima et al.), The Electrochemical Society, Pennington, NJ, 1997, Vol. 97–20.
193. G. Nogami, J. H. Kennedy, *J. Electrochem. Soc.* **1989**, *136*, 2583.
194. W. J. Albery, N. L. Dias, C. P. Wilde, *J. Electrochem. Soc.* **1987**, *134*, 601.
195. P. Herrasti, L. M. Peter, *J. Electroanal. Chem.* **1991**, *305*, 241.
196. J. Li, L. M. Peter, *J. Electroanal. Chem.* **1985**, *182*, 399.
197. B. H. Erné, D. Vanmaekelbergh, I. E. Vermeir, *Electrochim. Acta* **1993**, *38*, 2559.
198. J. Li, R. Peat, L. M. Peter, *J. Electroanal. Chem.* **1986**, *200*, 333.
199. R. Peat, L. M. Peter, *Electrochim. Acta* **1986**, *31*, 731.
200. R. Peat, L. M. Peter, *J. Electroanal. Chem.* **1986**, *209*, 307.
201. D. Vanmaekelbergh, J. J. Kelly, *J. Phys. Chem.* **1990**, *94*, 5406.
202. W. P. Gomes, S. Lingier, D. Vanmaekelbergh, *J. Electroanal. Chem.* **1989**, *269*, 237.
203. R. Tenne in *Semiconductor Micromachining: Fundamentals Electrochemistry and Physics* (Eds.: S. A. Campbell, H.-J. Lewerenz), John Wiley, New York, 1994, pp. 139–175, Vol. 1.
204. J. van de Ven, H. J. P. Nabben, *J. Electrochem. Soc.* **1990**, *137*, 1603.
205. G. A. Somorjai in *Chemistry in Two Dimensions: Surfaces*, Cornell University Press, Ithaca, NY, 1981.
206. S. Y. Huang, L. Kavan, I. Exnar et al., *J. Electrochem. Soc.* **1995**, *142*, L142.
207. J. G. Highfield, M. Grätzel, *J. Phys. Chem.* **1988**, *92*, 464.
208. B. O'Regan, M. Grätzel, D. Fitzmaurice, *Chem. Phys. Lett.* **1991**, *183*, 89.
209. B. O'Regan, M. Grätzel, D. Fitzmaurice, *J. Phys. Chem.* **1991**, *95*, 10525.
210. B. E. Conway, *J. Electrochem. Soc.* **1991**, *138*, 1539.
211. R. Könenkamp, R. Henninger, P. Hoyer, *J. Phys. Chem.* **1993**, *97*, 7328.
212. R. Könenkamp, R. Henninger, *Appl. Phys. A* **1994**, *58*, 87.
213. I. Bedja, S. Hotchandani, P. V. Kamat, *J. Phys. Chem.* **1996**, *100*, 19489.
214. G. Boschloo, D. Fitzmaurice, *J. Phys. Chem. B* **1999**, *103*, 2228.
215. F. Cao, G. Oskam, P. C. Searson et al., *J. Phys. Chem.* **1995**, *99*, 11974.
216. R. F. Howe, M. Grätzel, *J. Phys. Chem.* **1985**, *89*, 4495.
217. L. A. Lyon, J. T. Hupp, *J. Phys. Chem.* **1995**, *99*, 15718.
218. H. Lindström, S. Södergren, A. Solbrand et al., *J. Phys. Chem. B* **1997**, *101*, 7710.
219. H. Lindström, S. Södergren, A. Solbrand et al., *J. Phys. Chem. B* **1997**, *101*, 7717.
220. S. Lunell, A. Stashans, L. Ojamäe et al., *J. Am. Chem. Soc.* **1997**, *119*, 7374.
221. L. A. Lyon, J. T. Hupp, *J. Phys. Chem. B* **1999**, *103*, 4623.
222. R. van de Krol, A. Goossens, J. Schoonman, *J. Electrochem. Soc.* **1997**, *144*, 1723.
223. J. J. Kelly, D. Vanmaekelbergh, *Electrochim. Acta* **1998**, *43*, 2773.
224. A. Zaban, A. Meier, B. A. Gregg, *J. Phys. Chem. B* **1997**, *101*, 7985.
225. D. Vanmaekelbergh, P. E. de Jongh, *J. Phys. Chem. B* **1999**, *103*, 747.
226. H. Rensmo, H. Lindström, S. Södergren et al., *J. Electrochem. Soc.* **1996**, *143*, 3173.
227. G. Hodes, I. D. J. Howell, L. M. Peter, *J. Electrochem. Soc.* **1992**, *139*, 3136.
228. A. Hagfeldt, U. Björkstén, S.-E. Lindquist, *Sol. Energy Mater. Sol. Cells* **1992**, *27*, 293.
229. S. Södergren, A. Hagfeldt, J. Olsson et al., *J. Phys. Chem.* **1994**, *98*, 5552.
230. A. Shiga, A. Tsujiko, T. Ide et al., *J. Phys. Chem. B* **1998**, *102*, 6049.
231. K. Schwarzburg, F. Willig, *Appl. Phys. Lett.* **1991**, *58*, 2520.
232. P. E. de Jongh, D. Vanmaekelbergh, *Phys. Rev. Lett.* **1996**, *77*, 3427.

233. A. Solbrand, A. Henningson, S. Södergren et al., *J. Phys. Chem. B* **1999**, *103*, 1078.
234. A. Solbrand, H. Lindström, H. Rensmo et al., *J. Phys. Chem. B* **1997**, *101*, 2514.
235. K. Rajeshwar, *J. Appl. Electrochem.* **1985**, *15*, 1.
236. Y. Rosenwaks, B. R. Thacker, R. K. Ahrenkiel et al., *J. Phys. Chem.* **1992**, *96*, 10096.
237. S. Licht, V. Marcu, *J. Electroanal Chem.* **1986**, *210*, 197.
238. P. Singh, K. Rajeshwar, *J. Electrochem. Soc.* **1981**, *128*, 1724.
239. A. Heller, *Acc. Chem. Res.* **1981**, *14*, 154.
240. B. A. Parkinson, A. Heller, B. Miller, *Appl. Phys. Lett.* **1978**, *33*, 521.
241. B. J. Tufts, I. L. Abrahams, L. G. Casagrande et al., *J. Phys. Chem.* **1989**, *93*, 3260.
242. A. Heller, H. J. Leamy, B. Miller et al., *J. Phys. Chem.* **1983**, *87*, 3239.
243. K. Uosaki, Y. Shigematsu, H. Kita et al., *Anal. Chem.* **1989**, *61*, 1980.
244. M. J. Natan, J. W. Thackeray, M. S. Wrighton, *J. Phys. Chem.* **1986**, *90*, 4089.
245. J. W. Thackeray, M. J. Natan, P. Ng et al., *J. Am. Chem. Soc.* **1986**, *108*, 3570.
246. J. J. Hickman, M. S. Wrighton, *J. Am. Chem. Soc.* **1991**, *113*, 4440.
247. C. J. Murphy, A. B. Ellis, *J. Phys. Chem.* **1990**, *94*, 3082.
248. J. Z. Zhang, A. B. Ellis, *J. Phys. Chem.* **1992**, *96*, 2700.
249. C. J. Murphy, G. C. Lisensky, L. K. Leung et al., *J. Am. Chem. Soc.* **1990**, *112*, 8344.
250. S. Bastide, R. Butruille, D. Cahen et al., *J. Phys. Chem. B* **1997**, *101*, 2678.
251. C-M. Wang, A. Heller, H. Gerischer, *J. Am. Chem. Soc.* **1992**, *114*, 5230.
252. E. Aharon-Shalom, A. Heller, *J. Electrochem. Soc.* **1982**, *129*, 2865.
253. A. Heller, E. Aharon-Shalom, W. A. Bonner et al., *J. Am. Chem. Soc.* **1982**, *104*, 6942.
254. D. E. Aspnes, A. Heller, *J. Phys. Chem.* **1983**, *87*, 4919.
255. K. Rajeshwar, M. Kaneko, A. Yamada et al., *J. Phys. Chem.* **1985**, *89*, 806.
256. K. Rajeshwar, M. Kaneko, *J. Phys. Chem.* **1985**, *89*, 3587.
257. L. Thompson, J. DuBow, K. Rajeshwar, *J. Electrochem. Soc.* **1982**, *129*, 1934.
258. G. Hodes, L. Thompson, J. DuBow et al., *J. Am. Chem. Soc.* **1983**, *105*, 324.
259. A. W.-H. Mau, C-B. Huang, N. Kakuta et al., *J. Am. Chem. Soc.* **1984**, *106*, 6537.
260. C. Levy-Clement, A. Heller, W. A. Bonner et al., *J. Electrochem. Soc.* **1982**, *129*, 1701.
261. C. E. D. Chidsey, *Science* **1991**, *251*, 919.
262. J. F. Smalley, S. W. Feldberg, C. E. D. Chidsey et al., *J. Phys. Chem.* **1995**, *99*, 13141.
263. S. B. Sachs, S. P. Dudek, R. P. Hsung et al., *J. Am. Chem. Soc.* **1997**, *119*, 10563.
264. C. W. Sheen, J. X. Shi, J. Martensson et al., *J. Am. Chem. Soc.* **1992**, *114*, 1514.
265. Y. Gu, D. H. Waldeck, *J. Phys. Chem.* **1996**, *100*, 9573.
266. Y. Gu, D. H. Waldeck, *J. Phys. Chem. B* **1998**, *102*, 9015.
267. A. Haran, D. H. Waldeck, R. Naaman et al., *Science* **1994**, *263*, 948.
268. A. Hagfeldt, L. Walder, M. Grätzel, *Proc. Soc. Photo-Opt. Instrum. Eng.* **1995**, *2531*, 60.
269. H. Lindstrom, H. Rensmo, S.-E. Lindquist et al., *Thin Solid Films* **1998**, *323*, 141.
270. N. Kakuta, K. H. Park, M. F. Finlayson et al., *J. Phys. Chem.* **1985**, *89*, 732.
271. A. Ueno, N. Kakuta, K. H. Park et al., *J. Phys. Chem.* **1985**, *89*, 3828.
272. E. S. Smotkin, A. J. Bard, A. Campion et al., *J. Phys. Chem.* **1986**, *90*, 4604.
273. E. S. Smotkin, S. Cervera-March, A. J. Bard et al., *J. Phys. Chem.* **1987**, *91*, 6.
274. S. Kuwabata, N. Takahashi, S. Hirao et al., *Chem. Mater.* **1993**, *5*, 437.
275. C. S. C. Bose, K. Rajeshwar, *J. Electroanal. Chem.* **1992**, *333*, 235.
276. Y. Son, N. R. de Tacconi, K. Rajeshwar, *J. Electroanal. Chem.* **1993**, *345*, 135.
277. N. R. de Tacconi, Y. Son, K. Rajeshwar, *J. Phys. Chem.* **1993**, *97*, 1042.
278. N. R. Avvaru, N. R. de Tacconi, K. Rajeshwar, *Analyst* **1998**, *123*, 113.
279. S. Ito, T. Deguchi, K. Imai et al., *Electrochem. Solid State Lett.* **1999**, *2*, 440.
280. M. Zhou, W-Y. Lin, N. R. de Tacconi et al., *J. Electroanal. Chem.* **1996**, *402*, 221.
281. M. Zhou, N. R. de Tacconi, K. Rajeshwar, *J. Electroanal. Chem.* **1997**, *421*, 111.
282. N. R. de Tacconi, H. Wenren, K. Rajeshwar, *J. Electrochem. Soc.* **1997**, *144*, 3159.
283. N. R. de Tacconi, H. Wenren, D. McChesney et al., *Langmuir* **1998**, *14*, 2933.
284. N. R. de Tacconi, J. Carmona, K. Rajeshwar, to be published.
285. N. R. de Tacconi, M. Mrkic, K. Rajeshwar, *Langmuir* **2000**, *16*, 8426.
286. C. Anderson, A. J. Bard, *J. Phys. Chem. B* **1997**, *101*, 2611.

287. N. Takeda, M. Ohtani, T. Torimoto et al., *J. Phys. Chem. B* **1997**, *101*, 2644.
288. N. R. de Tacconi, K. Rajeshwar, R. O. Lezna, *Electrochim. Acta* **2000**, *45*, 3403.
289. N. R. de Tacconi, J. Carmona, K. Rajeshwar, *J. Phys. Chem. B* **1998**, *101*, 10151.
290. N. R. de Tacconi, J. Carmona, W. L. Balsam et al., *Chem. Mater.* **1998**, *10*, 25.
291. G. Hodes, J. Manassen, D. Cahen, *J. Appl. Electrochem.* **1977**, *7*, 182.
292. G. Hodes, J. Manassen, D. Cahen, *J. Electrochem. Soc.* **1977**, *127*, 544.
293. A. Fujishima, K. Honda, *Nature* **1972**, *238*, 37.
294. B. O'Regan, M. Grätzel, *Nature* **1991**, *353*, 737.
295. J. Manassen, G. Hodes, D. Cahen, *J. Electrochem. Soc.* **1977**, *124*, 532.
296. S. Licht, G. Hodes, R. Tenne et al., *Nature* **1987**, *326*, 863.
297. S. Licht, B. Wang, T. Soga et al., *Appl. Phys. Lett.* **1999**, *74*, 4055.
298. S. Licht, *J. Phys. Chem. B* **2001**, *105*, 6281.